

Numerical analysis of the weakly nonlinear Boussinesq system with a freely moving body on the bottom

Krisztian Benyo[†]

ABSTRACT: In this study, the numerical analysis of a specific fluid-solid interaction problem is detailed. The weakly nonlinear Boussinesq system is considered with the addition of a solid object lying on the flat bottom, allowed to move horizontally under the pressure forces created by the waves. We present an accurate finite difference scheme for this physical model, finely tuned to preserve important features of the original coupled system: nonlinear effects for the waves, energy dissipation due to the frictional movement of the solid. The moving bottom case is compared with a system where the same object is fixed to the bottom in order to observe the qualitative and quantitative differences in wave transformation. In particular a loss of wave amplitude is observed. The influence of the friction on the whole system is also measured, indicating differences for small and large coefficients of friction. Overall, hydrodynamic damping effects reminiscent to the dead-water phenomenon can be established.

Introduction

Understanding and predicting surface wave formations and their evolution has been one of the central elements of coastal engineering and oceanography for the past few decades. In 1871 Boussinesq introduced the first depth averaged model ([Bou71]). It originally described a physical situation with horizontal bottom and was later generalized for variable depths by Peregrine ([Per67]). These kind of models have played a crucial role in water wave modeling, especially in shallow water regions (such as the shoaling zone for a wave). From a mathematical point of view, these equations arise as shallow water asymptotic limits of the full water waves problem (for a thorough discussion on the subject, please refer to [Lan13]) and incorporate (weakly) dispersive and (weakly) nonlinear effects. Nowadays many reformulations and generalizations of the original Boussinesq system exist: for example Nwogu’s extended equation ([Nwo93]) or the abcd-system introduced in [BCS02], to cite a few of the most important ones.

Implementing a moving bottom in numerical models has its own challenges, experiments and tentatives to adapt existing (fixed bottom) shallow water models for a moving bottom regime appear from time to time in the literature. After observing successively generated solitary waves due to a disturbance in the bottom topography advancing at critical speed ([Wu87]) Wu et al. formally derived a set of generalized channel type Boussinesq systems ([TW92]), their work was extended later on in a formal study on more general long wave regimes ([Che03]). Tsunami research has also proved to be a main motivating factor with the consideration of water waves type problems with a moving bottom, for the full justification of the general problem in shallow water asymptotic regimes, we refer to [Igu11].

The scope of the current work revolves around a model in which the bottom is still moving, but its movement is not prescribed, instead it is generated by the wave motion, introduced in the author’s previous work ([Ben17]). The main idea is to place a freely moving object on the bottom of the fluid domain, its movement being governed by the wave motions. Physical motivations for such a model stem, for example, from marine energy engineering, most notably submerged wave energy converters (submerged pressure differential devices, [AELS14] and references therein) and oscillating wave surge converters (WaveRollers and Submerged plate devices, [GIL⁺14]). Originating from the same context, one can also handle the “complementary” problem in which the waves are interacting with a freely moving floating structure. The theoretical background of such problems have been extensively analyzed in recent years, see for example [Lan17], [Boc18].

[†]Institut de Mathématiques de Bordeaux, Université de Bordeaux, France. (krisztian.benyo@math.u-bordeaux.fr)

Although the numerical study of immersed structures is not entirely new, our approach is heavily based on a theoretical analysis of the general system, rather than experimental or numerical considerations usually present in the corresponding bibliography. An approach with numerous physical and biological applications was developed by Cottet et al. ([CM06], [CMM08]) based on a level set formulation, adapting an immersed boundary method and general elasticity theory (see also [FGG07]). Modeling underwater landslides provides for an excellent example of such systems, we refer to [DK13] and references therein for recent developments. Numerical models adapted to tsunami generation due to seabed deformations were presented for example in [GN07] or [Mit09]. From a control theory point of view, Zuazua et al. ([DNZ15]) performed an analytical and numerical analysis on underwater wave generator models. Perhaps one of the most relevant existing studies concerns a submerged spring-block model and the associated experimental and numerical observations ([AMMM15], [ACDNn17]).

The structure of the article is as follows. After a brief introduction, we present the weakly nonlinear Boussinesq system in a fluid domain with a flat bottom topography and with a solid object lying on the bottom, capable of moving horizontally under the pressure forces created by the waves. Following our previous work, this coupled system admits a unique solution for a long time scale ([Ben17]).

In the third section we detail the finite difference numerical scheme adapted to this system. We elaborate a fourth order accurate staggered grid system for the variables concerning the movement of the fluid, following the footsteps of Lin and Man ([LM07]). As for the time discretization, an adapted fourth order accurate Adams–Bashforth predictor-corrector method is implemented, incorporating the discretized ordinary differential equation characterizing the solid displacement via a modified central finite difference scheme. We end this section with some remarks on the boundary conditions implemented and on certain useful properties of our adaptation.

Section 4 details the numerical experiments concerning the model. The convergence of the finite difference scheme is measured to be almost of order 4 in time and in space for a flat bottom as well as for large coefficients of friction, greatly improving the reference staggered grid model (of order 2 only) in [LM07] over a flat bottom. An order 3 mesh convergence and an order 2 convergence in time is observed for small coefficients of friction. The transformation of a passing wave over the solid is detailed in various different physical regimes. Wave shoaling effects are examined and compared to a system with the same parameters admitting a fixed solid object on the bottom instead of a freely moving one. The effects of the friction on the motion of the solid are also measured, revealing that the solid comes to a halt after the wave has passed over it. Measuring the solid motion also indicates hydrodynamical damping effects reminiscent to the ones attributed to dead-water phenomena, closely tied to internal wave generation (for more details, we refer to [Ekm04], [MVD10], [Duc12]). Long term effects by a wave train test are also presented at the end of the section.

1 The governing equations

1.1 The physical regime

We are going to work in two spatial dimensions, and we will reference the horizontal coordinate by x and the vertical coordinate by z . The time parameter shall be $t \in \mathbb{R}^+$. The physical domain of the fluid is

$$\Omega_t = \{(x, z) \in \mathbb{R} \times \mathbb{R} : -H_0 + b(t, x) < z < \zeta(t, x)\},$$

where H_0 is a parameter of the system measuring the base water depth and the functions $\zeta(t, x)$ and $b(t, x)$ stand for the free surface elevation and the bottom topography variation respectively (see Figure 1).

The solid on the bottom is supposed to be moving only in a horizontal direction, its displacement vector is denoted by $X(t)$, consequently its velocity is given by $v(t) = \dot{X}(t)$. Therefore we have that

$$b(t, x) = \mathfrak{b}(x - X(t)), \tag{1.1}$$

with \mathbf{b} corresponding to the initial state of the solid, at $t = 0$, thus assuming that $X(0) = 0$. This function \mathbf{b} is of class $\mathcal{C}^\infty(\mathbb{R})$ and compactly supported.

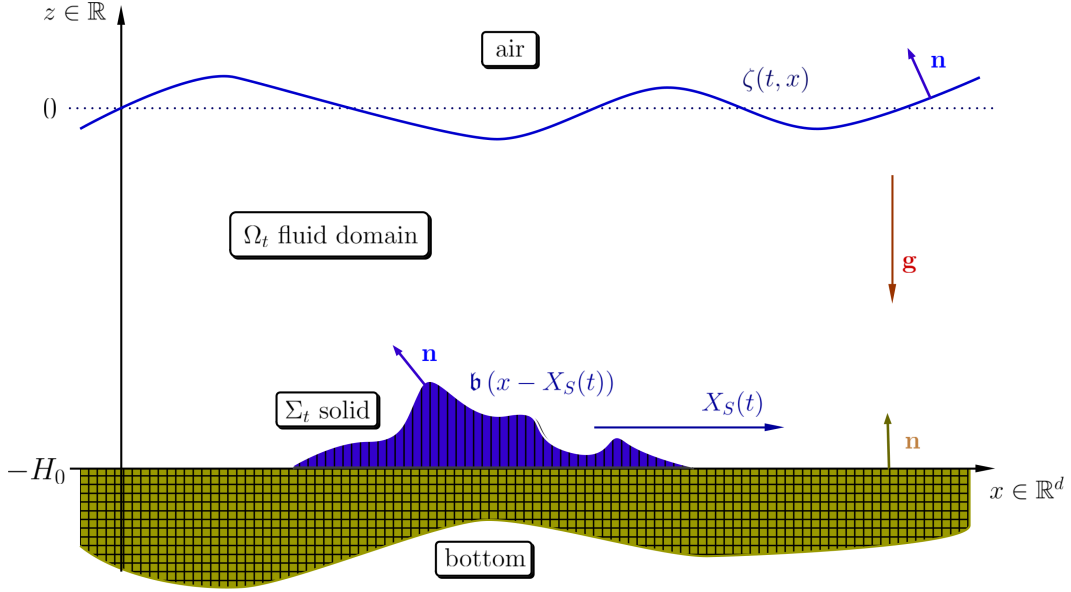


Figure 1: The coupled water waves setting in the presence of a solid

The fluid is assumed to be homogeneous, inviscid, incompressible, and irrotational. Its dynamics in general are described by the full water waves problem, based on the free surface Euler equations (see for instance [Lan13]).

The solid is supposed to be rigid and homogeneous with a given mass M , in frictional contact with the flat bottom of the domain. Its movement is governed by Newton's second law.

Since the weakly nonlinear Boussinesq equation is a shallow water asymptotic equation, we have to introduce characteristic scales of the problem. First of all H_0 denotes the base water depth, and L , the characteristic horizontal scale of the wave motion as well as the solid size. Moreover we have a_{surf} , the order of the free surface amplitude, and a_{bott} , the characteristic height of the solid.

Using these quantities, we can introduce several dimensionless quantities:

- shallowness parameter $\mu = \frac{H_0^2}{L^2}$,
- nonlinearity (or amplitude) parameter $\varepsilon = \frac{a_{surf}}{H_0}$,
- bottom topography parameter $\beta = \frac{a_{bott}}{H_0}$,

which will play an important role in the formulation of the governing equations.

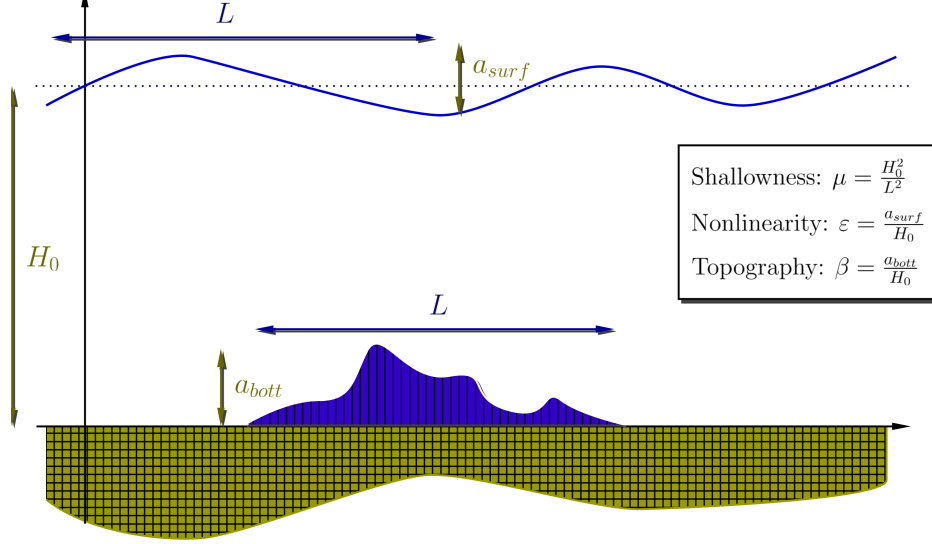


Figure 2: The characteristic scales of the coupled water waves problem

1.2 The coupled Boussinesq system

We consider here a weakly nonlinear regime, i.e. we assume that $\varepsilon = \mathcal{O}(\mu)$ and we suppose that the scale of the solid is relatively small (meaning $\beta = \mathcal{O}(\mu)$). The fluid is then governed by a Boussinesq system. Thus, the asymptotic regime writes as

$$0 \leq \mu \leq \mu_{max} \ll 1, \quad \varepsilon = \mathcal{O}(\mu), \quad \beta = \mathcal{O}(\mu). \quad (\text{BOUS})$$

Under the Boussinesq regime (BOUS) the governing fluid equations at order $\mathcal{O}(\mu^2)$ take the form of

$$\begin{cases} \partial_t \zeta + \partial_x (h \bar{V}) = \frac{\beta}{\varepsilon} \partial_t b, \\ \left(1 - \frac{\mu}{3} \partial_{xx}\right) \partial_t \bar{V} + \partial_x \zeta + \varepsilon (\bar{V} \cdot \partial_x) \bar{V} = -\frac{\mu \beta}{2\varepsilon} \partial_x \partial_t^2 b. \end{cases} \quad (1.2)$$

with the nondimensionalized fluid height function $h = 1 + \varepsilon \zeta - \beta b$ and the vertically averaged horizontal velocity

$$\bar{V}(t, x) = \frac{1}{h} \int_{-1+\beta b}^{\varepsilon \zeta} V(t, x, z) dz,$$

with V being the horizontal component of the velocity field of the fluid. In the equation, the variables are the nondimensionalized forms of the corresponding physical quantities described in the previous section. To recover the quantities with the proper dimensions, it is enough to multiply the variable by its corresponding characteristic scale.

Remark 1.1. *Without the smallness assumption on ε , and on β , it is still possible to perform an asymptotic expansion at $\mathcal{O}(\mu^2)$. The resulting system is more general than the Boussinesq system (1.2) but also more complicated, it is known as the Serre–Green–Naghdi equations (see for example [HI15]).*

Following the derivation presented in [Ben17], Newton's second law for the solid displacement can be written as

$$\ddot{X} = -\frac{c_{fric}}{\sqrt{\mu}} F_{normal}(X, \zeta) \frac{\dot{X}}{|\dot{X}| + \delta} + \frac{\varepsilon}{\bar{M}} \int_{\mathbb{R}} \zeta \partial_x b dx, \quad (1.3)$$

with

$$F_{normal}(X, \zeta) = 1 + \frac{c_{solid}}{\beta} + \frac{\varepsilon}{\beta \bar{M}} \int_{\text{supp}(b)+X} \zeta dx, \quad (1.4)$$

where we grouped together the quantities depending only on the physical parameters of the solid:

$$c_{solid} = \frac{|\text{supp}(\mathbf{b})|}{\tilde{M}} \left(\frac{P_{atm}}{\rho g H_0} + 1 \right) - \frac{\beta}{\tilde{M}} \int_{\text{supp}(\mathbf{b})} b \, dx, \quad (1.5)$$

as well as

$$\tilde{M} = \frac{M}{\rho L a_{bott}}.$$

Apart from the smallness parameters originating from the system describing the fluid dynamics (equations (1.2)), another important parameter in the numerical analysis is the coefficient of friction c_{fric} . The actual measurement of this coefficient is rather difficult, especially in a complex physical system such as the current one, mainly because its value depends on many other physical parameters (like the material structure of the surfaces, the temperature, the pressure, the velocity of the sliding, etc.). Generally speaking a coefficient of $10^{-2} \sim 10^{-3}$ corresponds to a relatively frictionless sliding, and values in the range of 1 signify an important friction between the contact media.

Moreover, δ is an artificial parameter to introduce a uniform dynamical friction law for the movement, its value is taken to be sufficiently small ($\sim 10^{-10}$) in order to be much smaller than any physically meaningful solid velocity value. Finally, we have that P_{atm} stands for the atmospheric pressure and g the gravitational acceleration constant.

Remark 1.2. *The first term in c_{solid} corresponds to the effect of the atmospheric and hydrostatic pressure. It is reasonable to assume that these two effects should be comparable, which means that for the scale of the base water depth H_0 we can infer that*

$$\frac{P_{atm}}{\rho g H_0} + 1 = \frac{10m}{H_0} + 1,$$

implying that for small depths (~ 1 m) the atmospheric pressure dominates over even the hydrostatic effects by a factor of 10, resulting in negligible hydrostatic effects which is not ideal for our analysis.

To sum it up, the free surface equations with a solid moving at the bottom in the case of the Boussinesq approximation take the following form

$$\begin{cases} \partial_t \zeta + \partial_x(h\bar{V}) = \frac{\beta}{\varepsilon} \partial_t b, \\ \left(1 - \frac{\mu}{3} \partial_{xx}\right) \partial_t \bar{V} + \partial_x \zeta + \varepsilon(\bar{V} \cdot \partial_x) \bar{V} = -\frac{\mu\beta}{2\varepsilon} \partial_x \partial_{tt} b, \\ \ddot{X} = -\frac{c_{fric}}{\sqrt{\mu}} F_{normal}(\zeta, X) \frac{\dot{X}}{|\dot{X}| + \delta} + \frac{\varepsilon}{\tilde{M}} \int_{\mathbb{R}} \zeta \partial_x b \, dx. \end{cases} \quad (1.6a)$$

$$\quad (1.6b)$$

With the numerical scheme in mind, we can rewrite this system in a more compact form as follows

$$\begin{cases} \partial_t \zeta = E(\zeta, \bar{V}, X, \dot{X}), \\ \partial_t \bar{U} = F(\zeta, \bar{V}, X, \dot{X}, \ddot{X}), \\ \ddot{X} = G(\zeta, X, \dot{X}), \end{cases} \quad (1.7a)$$

$$\quad (1.7b)$$

where

$$\bar{U} = \bar{U}(\bar{V}) = \bar{V} - \frac{\mu}{3} \partial_{xx} \bar{V}. \quad (1.8)$$

The remaining terms are given by

$$E(\zeta, \bar{V}, X, \dot{X}) = -\partial_x(h\bar{V}) - \frac{\beta}{\varepsilon} \partial_x \mathbf{b}(x - X) \dot{X}, \quad (1.9a)$$

$$F(\zeta, \bar{V}, X, \dot{X}, \ddot{X}) = -\partial_x \zeta - \frac{\varepsilon}{2} \partial_x(\bar{V}^2) - \frac{\mu\beta}{2\varepsilon} \partial_{xxx} \mathbf{b}(x - X) (\dot{X})^2 + \frac{\mu\beta}{2\varepsilon} \partial_{xx} \mathbf{b}(x - X) \ddot{X} \quad (1.9b)$$

$$G(\zeta, X, \dot{X}) = -\frac{c_{fric}}{\sqrt{\mu}} F_{normal}(\zeta, X) \frac{\dot{X}}{|\dot{X}| + \delta} + \frac{\varepsilon}{\tilde{M}} \int_{\mathbb{R}} \zeta \partial_x \mathbf{b}(x - X) \, dx \quad (1.9c)$$

1.3 Relevant properties of the system

Due to the special structure of our system, let us define the following adapted Banach-space to provide a uniformly formulated energy estimate.

Definition 1.1. *The Sobolev type space \mathcal{X}^s is given by*

$$\mathcal{X}^s(\mathbb{R}) = \left\{ \mathcal{U} = (\zeta, \bar{V}) \in L^2(\mathbb{R}) \text{ such that } \|\mathcal{U}\|_{\mathcal{X}^s} < \infty \right\},$$

where

$$\|\mathcal{U}\|_{\mathcal{X}^s} = \|\zeta\|_{H^s} + \|\bar{V}\|_{H^s} + \sqrt{\mu} \|\partial_x \bar{V}\|_{H^s}.$$

The last term in the \mathcal{X}^s norm appeared due to the necessity to control the dispersive smoothing.

By introducing the wave-structure energy functional

$$E_B(t) = \frac{1}{2} \int_{\mathbb{R}} \zeta^2 dx + \frac{1}{2} \int_{\mathbb{R}} h(\bar{V})^2 dx + \frac{1}{2} \int_{\mathbb{R}} \frac{\mu}{3} h(\partial_x \bar{V})^2 dx + \frac{1}{2\varepsilon} |\dot{X}|^2, \quad (1.10)$$

we can establish an L^2 type energy estimate for the coupled system (1.6), from which we are able to deduce a certain control on the velocity of the solid.

We have the following ([Ben17]):

Proposition 1.1. *Let $\mu \ll 1$ sufficiently small and $s_0 > 1$. Then any $\mathcal{U} \in \mathcal{C}^1([0, T] \times \mathbb{R}) \cap \mathcal{C}^1([0, T]; H^{s_0})$, $X \in \mathcal{C}^2([0, T])$ satisfying the coupled system (1.6), with initial data $\mathcal{U}(0, \cdot) = \mathcal{U}_{in} \in \mathcal{C}^1(\mathbb{R}) \cap H^{s_0}$ and $(X(0), \dot{X}(0)) = (0, v_{S_0}) \in \mathbb{R} \times \mathbb{R}$ verifies the energy estimate*

$$\sup_{t \in [0, T]} \left\{ e^{-\sqrt{\varepsilon} c_0 t} E_B(t) \right\} \leq 2E_B(0) + 2\mu c_0 T \|\mathfrak{b}\|_{H^3}^2, \quad (1.11)$$

where

$$c_0 = c(\|\mathcal{U}\|_{T, W^{1, \infty}}, \|\mathcal{U}\|_{T, H^{s_0}}, \|\mathfrak{b}\|_{W^{3, \infty}}).$$

Corollary 1.1. *This energy estimate provides us with a natural control on the solid velocity, namely*

$$\sup_{t \in [0, T]} \left\{ e^{-\sqrt{\varepsilon} c_0 t} |\dot{X}(t)|^2 \right\} \leq \varepsilon \|\mathcal{U}_{in}\|_{\mathcal{X}^0}^2 + \varepsilon |v_{S_0}|^2 + \varepsilon \mu c_0 T \|\mathfrak{b}\|_{H^3}^2, \quad (1.12)$$

where c_0 is as before.

Since we intend to adapt a similar dissipative property for our numerical scheme, we present here the brief outline of this proposition.

A sketch of the proof: It follows a standard energy estimate argument; we multiply the first equation of (1.6) by ζ and the second equation by $h\bar{V}$, and we integrate over \mathbb{R} with respect to x .

Handling the right hand side of the first equation is the key to uniform estimates, since the integral term

$$- \int_{\mathbb{R}} \zeta \partial_x b dx \cdot \dot{X},$$

that appears following the multiplication and the integration is also present in the right hand side of the solid equation (1.6b) multiplied by \dot{X} . Using this equality one can estimate the integral simply by $\tilde{M}\varepsilon^{-1} \dot{X} \dot{X}$ since the new friction term is nonpositive.

The rest of the proof is only straightforward term-by-term estimates, paying close attention to the higher order derivatives $((1 - \frac{\mu}{3} \partial_{xx}) \partial_t \bar{V})$ in the momentum equation and its source term $(\partial_x \partial_{tt} b)$.

The existence and uniqueness theorem for the coupled Boussinesq system then states as follows (for more details, please refer to [Ben17]):

Theorem 1.1. *Let us consider the coupled system defined by equations (1.6). Let us suppose that for the initial value ζ_{in} and \mathbf{b} the lower bound condition (1.13)*

$$\exists h_{min} > 0, \forall Y \in \mathbb{R}, 1 + \varepsilon \zeta_{in}(Y) - \varepsilon \mathbf{b}(Y) \geq h_{min} \quad (1.13)$$

is satisfied. If the initial values ζ_{in} and \bar{V}_{in} are in $\mathcal{X}^s(\mathbb{R})$ with $s \in \mathbb{R}$, $s > 3/2$, and $V_{S_0} \in \mathbb{R}$ then there exists a maximal $T_0 > 0$ independent of ε such that there is a unique solution

$$\begin{aligned} (\zeta, \bar{V}) &\in C\left(\left[0, \frac{T_0}{\sqrt{\varepsilon}}\right]; \mathcal{X}^s(\mathbb{R})\right) \cap C^1\left(\left[0, \frac{T_0}{\sqrt{\varepsilon}}\right]; \mathcal{X}^{s-1}(\mathbb{R})\right), \\ X &\in C^2\left(\left[0, \frac{T_0}{\sqrt{\varepsilon}}\right]\right) \end{aligned}$$

with uniformly bounded norms for the system (1.6) with initial conditions $(\zeta_{in}, \bar{V}_{in})$ and $(0, \sqrt{\varepsilon}V_{S_0})$.

2 The discretized model

In this section we present the elements of the discretized scheme. We follow the ideas of Lin and Man ([LM07]) for a staggered grid approach. We improve their model by aiming for a fourth order overall accuracy for the quantities characterizing the fluid dynamics and the time stepping in general. In light of the a priori estimate in Proposition 1.1. we will examine the dissipative property of the discretized solid equation (Lemma 2.1).

2.1 The finite difference scheme on a staggered grid

Since the solid movement is time dependent only ($X(t)$ does not depend on the horizontal coordinate x), spatial discretization only concerns the fluid variables, for which we aim for a fourth order precision.

In their article, Lin and Man obtained a stable and accurate model for a Boussinesq type system (the Nwogu equations). They observed good conservative properties for the fluid system, attributed mainly to the staggered grid method they implemented, which is an important factor for long-term measurements, furthermore it is well-adapted to accurate energy measurements of the system.

We implement their staggered grid method in which the “scalar” quantities, such as the surface elevation ζ , the bottom topography b and the fluid height h , are defined on the grid points, and the “vectorial” variable, the averaged velocity \bar{V} (that is still a scalar since we are only working in one horizontal dimension) is defined on the mid-points of the mesh. The mesh size will be chosen as Δx , numbered by $i = 1, 2, \dots, N_{space}$. The discrete equation for ζ (based on (1.9a)) will be defined for mesh points and the equation for \bar{V} (from equation (1.9b)) for the mid-points.

In order to be able to do this, we will have to define the “scalar” quantities for the mid-points as well, we shall do so by a four point centered fourth order interpolation, that is,

$$\zeta_{i+1/2} = \frac{-\zeta_{i-1} + 9\zeta_i + 9\zeta_{i+1} - \zeta_{i+2}}{16}.$$

In the reference article [LM07], only a linear interpolation was used. Even though it was not mentioned at all, we believe it to be one of the main reasons for the loss of mesh convergence in their scheme.

For the spatial discretization in general, we chose fourth order accurate central finite difference schemes for the different orders of derivatives. In their work, Lin and Man chose only second order schemes for the higher order derivatives which is another reason for the resulted loss in mesh convergence in their case. In our implementation even higher order derivatives are discretized by fourth order schemes.

Observing the right hand sides of equations (1.7a) we may separate four different types of terms. Once again, we emphasize on the fact that the first equation will act on mesh points while the second one will be defined on mid-points of the grid.

- First order derivative on grid points for a “scalar” quantity, this concerns the term $\partial_x \mathbf{b}$, and equivalently first order derivative on mid-points for “vectorial” variables, this concerns the term $\partial_x(\bar{V}^2)$. For this case, the classical four point central difference scheme of order 4 writes as

$$(\partial_x \mathbf{b})_i = \frac{\mathbf{b}_{i-2} - 8\mathbf{b}_{i-1} + 8\mathbf{b}_{i+1} - \mathbf{b}_{i+2}}{12\Delta x}, \quad (2.1)$$

and similarly for the derivative of \bar{V}^2 with mid-points.

- First order derivative on mid-points for a quantity having values in grid points, this concerns the term $\partial_x(h\bar{V})$, and equivalently first order derivative on grid points for quantities having values in mid-points, this concerns the term $\partial_x \zeta$. For this case, the adapted four point central difference scheme of order 4 writes as

$$(\partial_x \zeta)_{i+1/2} = \frac{\zeta_{i-1} - 27\zeta_i + 27\zeta_{i+1} - \zeta_{i+2}}{24\Delta x}, \quad (2.2)$$

and similarly for the derivative of $h\bar{V}$ with mid-points.

- Second order derivative on mid-points for quantities having values at grid points, this concerns both $\partial_{xx} \mathbf{b}$ and $\partial_{xx} \bar{V}$. A classical fourth order accurate central finite difference scheme is implemented, meaning

$$(\partial_{xx} \mathbf{b})_{i+1/2} = \frac{-\mathbf{b}_{i-3/2} + 16\mathbf{b}_{i-1/2} - 30\mathbf{b}_{i+1/2} + 16\mathbf{b}_{i+3/2} - \mathbf{b}_{i+5/2}}{12(\Delta x)^2}, \quad (2.3)$$

and similarly for \bar{V} .

- Third order derivative on mid-points for a term having values on grid points, this concerns $\partial_{xxx} \mathbf{b}$. Once again, a fourth order accurate central scheme is applied,

$$(\partial_{xxx} \mathbf{b})_{i+1/2} = \frac{\mathbf{b}_{i-5/2} - 8\mathbf{b}_{i-3/2} + 13\mathbf{b}_{i-1/2} - 13\mathbf{b}_{i+3/2} + 8\mathbf{b}_{i+5/2} - \mathbf{b}_{i+7/2}}{8(\Delta x)^3}. \quad (2.4)$$

The high accuracy guarantees that we can capture more precisely the nonlinear interaction between the fluid and the solid without posing problems for the numerical scheme due to the necessity of information on many grid points, since the solid is localized to its support (the middle section of the wave tank, as explained in Section 2.4).

2.2 Time stepping with Adams–Bashforth

As elaborated in [LM07], we adapt a fourth order accurate Adams predictor-corrector method. Starting from the initial condition at time $t = 0$, the first two values of the quantities may be generated by a fourth order classic Runge–Kutta (RK4) time stepping algorithm. Let us suppose that currently we are at time step $n \geq 2$ and as such, all information on the main variables (ζ , \bar{V} , and X) is known. The method consists of two steps:

1. First, the predictor step is implemented on the fluid equations (equations (1.7a)) by the explicit third order Adams–Bashforth scheme

$$\begin{aligned} \zeta_i^{n+1*} &= \zeta_i^n + \frac{\Delta t}{12} (23E_i^n - 16E_i^{n-1} + 5E_i^{n-2}), \\ \bar{U}_{i+1/2}^{n+1*} &= \bar{U}_{i+1/2}^n + \frac{\Delta t}{12} (23F_{i+1/2}^n - 16F_{i+1/2}^{n-1} + 5F_{i+1/2}^{n-2}), \end{aligned}$$

in addition we apply the algorithm for calculating the solid position (presented in the following section),

$$X^{n+1} = \bar{G}(\zeta^n, X^n, X^{n-1}, X^{n-2}). \quad (2.5)$$

2. With the knowledge of the predicted values, the next step is the correction by a fourth order Adams–Moulton method

$$\begin{aligned}\zeta_i^{n+1} &= \zeta_i^n + \frac{\Delta t}{24} \left(9E(\zeta_i^{n+1*}, \bar{V}_{i+1/2}^{n+1*}, X^{n+1}) + 19E_i^n - 5E_i^{n-1} + E_i^{n-2} \right), \\ \bar{U}_{i+1/2}^{n+1} &= \bar{U}_{i+1/2}^n + \frac{\Delta t}{24} \left(9F(\zeta_i^{n+1*}, \bar{V}_{i+1/2}^{n+1*}, X^{n+1}) + 19F_{i+1/2}^n - 5F_{i+1/2}^{n-1} + F_{i+1/2}^{n-2} \right).\end{aligned}$$

Remark 2.1. *Additionally, the predictor-corrector method can be iterated to guarantee even more accuracy for the algorithm.*

We remark that in [LM07], the same algorithm was used for the determination of the fluid quantities, and in the end the method was presented, without any explications, as a method with a convergence of order 2 instead of the theoretical order 4 in the time variable. One of the reasons for their loss of convergence can be the negative effects of a second order discretization in the spatial variable on a fourth order in time scheme. Another likely scenario would entail a not too accurate generation of the initial steps, indeed the predictor-corrector algorithm requires the first two steps to be generated by another algorithm, implying that if one were to use less accurate methods for the initial steps, that could negatively influence the convergence in time. Since in their case, it was not described how they obtained the first few steps, this can not be excluded.

2.3 Time discretization for the solid movement

Equation (1.7b) is an ODE which involves no further spatial discretization. We shall discretize it in time, considering a time step Δt indexed by $n = 1, 2, \dots, N_{time}$. We have to be careful though, since this equation is coupled to the first two equations of the system, having the source terms depending on X , \dot{X} , and \ddot{X} as well, and as such it is incorporated in the Adams scheme presented in the previous section.

Notice the presence of integrals of the fluid variables in the expression $G(\zeta, X, \dot{X})$ which implies some restrictions for calculating the numerical integral since these variables are only known for grid and mid-points. For further details, please refer to Section 2.5.

Another remark concerns the order of magnitude of the two terms of G . We are working with a regime where the shallowness parameter μ is supposed to be small, meaning that the first term is at least of order $\mathcal{O}(\mu^{-1/2})$ while the second term is small, of order $\mathcal{O}(\mu)$. As explained in Proposition 1.1. we have a strong control on the solid velocity, moreover good dissipative properties for the coupled system. We want to achieve a similar property for the discretized system, that is a similar dissipation of the discrete energy which in turn ensures that oscillations or other instabilities do not appear in the simulation.

First of all, we can write that

$$G(\zeta, X, \dot{X}) = -C(\zeta, X) \frac{\dot{X}}{|\dot{X}| + \delta} + \bar{C}(\zeta, X), \quad (2.6)$$

where we introduced the following two quantities

$$C(\zeta, X) = \frac{c_{fric}}{\sqrt{\mu}} \left(1 + \frac{c_{solid}}{\beta} + \frac{\varepsilon}{\tilde{M}\beta} \int_{\text{supp}(\mathbf{b})+X} \zeta \, dx \right), \quad (2.7a)$$

$$\bar{C}(\zeta, X) = \frac{\varepsilon}{\tilde{M}} \int_{\mathbb{R}} \zeta \partial_x \mathbf{b}(x - X) \, dx. \quad (2.7b)$$

We wish to construct an appropriate numerical scheme. Let us suppose that we are at time step n , so that quantities ζ^n , \bar{V}^n , and X^n are known up until the index n . This implies that the constants $C^n = C(\zeta^n, X^n)$ and $\bar{C}^n = \bar{C}(\zeta^n, X^n)$ are also known (since they do not involve any time differentiation).

We base our discretization on the reformulation (2.6) of the equation at hand. Let us apply a second order accurate central finite difference scheme on the acceleration \ddot{X} and on the velocity \dot{X} , furthermore let us apply a second order accurate backwards finite difference scheme for its absolute value $|\dot{X}|$.

This yields

$$\frac{X^{n+1} - 2X^n + X^{n-1}}{(\Delta t)^2} = -C^n \frac{\frac{X^{n+1} - X^{n-1}}{2\Delta t}}{\left| \frac{3X^n - 4X^{n-1} + X^{n-2}}{2\Delta t} \right| + \delta} + \bar{C}^n, \quad (2.8)$$

so by rearranging the terms we get that

$$\begin{aligned} & \left(1 + (\Delta t)^2 \frac{C^n}{|3X^n - 4X^{n-1} + X^{n-2}| + 2\Delta t\delta} \right) X^{n+1} \\ &= 2X^n - \left(1 - (\Delta t)^2 \frac{C^n}{|3X^n - 4X^{n-1} + X^{n-2}| + 2\Delta t\delta} \right) X^{n-1} + (\Delta t)^2 \bar{C}^n. \end{aligned} \quad (2.9)$$

Notice that by the definition of C , the factor of X^{n+1} is strictly positive, thus we may multiply by its inverse to obtain an explicit formula for X^{n+1} , namely

$$X^{n+1} = \bar{G}(\zeta^n, X^n, X^{n-1}, X^{n-2}), \quad (2.10)$$

where

$$\bar{G}(\zeta^n, X^n, X^{n-1}, X^{n-2}) = \frac{2X^n - \left(1 - (\Delta t)^2 \frac{C^n}{|3X^n - 4X^{n-1} + X^{n-2}| + 2\Delta t\delta} \right) X^{n-1} + (\Delta t)^2 \bar{C}^n}{1 + (\Delta t)^2 \frac{C^n}{|3X^n - 4X^{n-1} + X^{n-2}| + 2\Delta t\delta}}.$$

Remark 2.2. Notice that we choose the same order for the central finite difference schemes for the first and second order derivatives. The accuracy of the backwards finite difference scheme for the absolute value of the velocity estimate was chosen accordingly, and may be adapted.

The important property of this discretization is that the discrete equation verifies a certain a priori estimate, just like the one presented in Corollary 1.1.

Lemma 2.1. Owing to equation (2.8), the velocity associated to the displacement

$$\dot{X}^n := \frac{X^{n+1} - X^{n-1}}{2\Delta t} \quad (2.11)$$

verifies the following

$$|\dot{X}^n| \leq \bar{C}^n n \Delta t + \mathcal{O}((\Delta t)^2). \quad (2.12)$$

Proof: Let us multiply equation (2.8) by \dot{X}^n . Then, we obtain

$$\frac{(X^{n+1} - X^n)^2 - (X^n - X^{n-1})^2}{2(\Delta t)^3} = -C^n \frac{(\dot{X}^n)^2}{\left| \frac{3X^n - 4X^{n-1} + X^{n-2}}{2\Delta t} \right| + \delta} + \bar{C}^n \dot{X}^n.$$

Notice first of all that the first term on the right hand side is non-positive. Moreover, on the left hand side we have a second order approximation of the value $\partial_t((\dot{X})^2)(n\Delta t)$, as such we may replace it with another second order approximation, namely $\partial_t((\dot{X}^n)^2)$ modulo an error term of order $\mathcal{O}((\Delta t)^2)$. Combining these two remarks, we get that

$$\partial_t((\dot{X}^n)^2)(t)^2 \leq \bar{C}^n \dot{X}^n + \mathcal{O}((\Delta t)^2). \quad (2.13)$$

A Grönwall type inequality allows us to conclude in the desired way. \square

2.4 The wave tank and its boundaries

Notice that the weakly nonlinear Boussinesq system (1.2) has its domain of validity for $x \in \mathbb{R}$ which is clearly not the case for numerical models. Hence we consider the discretized model in a wave tank of sufficiently large size (it shall be detailed for each experiment in the next section). The idea is to place the solid in the middle of the tank and numerically generate the waves (soliton or wave train) near the

solid, therefore allowing us to focus on the middle section of the tank, the effects of boundary conditions imposed on the horizontal limits would be negligible.

In all the cases, the width of the wave tank is taken to be at least $100L$ with L being the wavelength of a wave, and the analysis is focused on the central $20L \sim 30L$ wide region of the domain.

As for the boundary conditions, for the sake of clarity, solid walls are implemented, implying reflective boundaries for the fluid variables. This means Neumann-type boundary condition for the “scalar” parameters ζ and h (the derivative equals to 0) and Dirichlet-type boundary condition on the fluid velocity \bar{V} (equaling to 0).

Variables for the solid are not concerned by these limiting conditions since they are independent of the spatial variable. The only technical effect is that the simulation is to be stopped when the object touches the boundary. As evoked before, due to the size of the wave tank, it is not a likely scenario.

2.5 Further remarks

The first remark concerns a reference solution for the Boussinesq system with completely flat bottom topography. It is known that a solitary wave solution (soliton) exists for this equation (see for example [BC16]). Naturally, by introducing a solid object on the bottom of the fluid domain, this referential solution will not stay a solitary wave propagating at a constant speed, it will be transformed, deformed according to the governing equations and the change in bottom topography. Nevertheless it serves as a basic tool to analyze the effects of the object on a single wave, as it will be done during the first half of the next section.

Some words should be mentioned about the effect of the solid displacement X on the fluid equations in (1.6a). Due to the horizontal motion of the object, it is present in the variable b as a translation. Since there are multiple instances when derivatives of the bottom topography function are taken, the order of the operations has to be established with respect to the discretization.

In our algorithm, at each time step, the actual bottom surface shall be calculated via the translation by X^n of the initial state \mathbf{b} and then it is discretized on the grid points and the mid-points as well. If we were to discretize the initial bottom topography and then translate it, it is clear that the fitting of the translated discrete bottom to the actual grid would create additional error terms which could potentially decrease the overall accuracy.

However we shall mention that our approach works mainly because the initial bottom surface \mathbf{b} as a function defined on \mathbb{R} is known, so that we can discretize any translated instance of it. It would not be possible without accurate interpolations, if the solid height was initially given only on grid points.

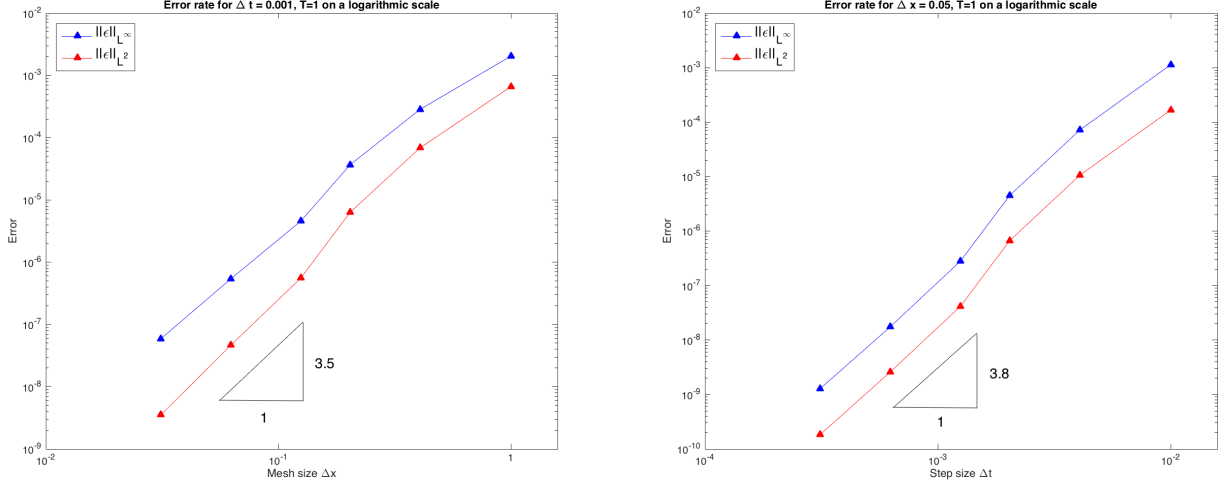
An important remark concerns the integral terms present in the solid equation (1.3). Except for the volume of the solid, these integrals involve integration over the support of the object (at its current state) of fluid variables that are initially only defined on mesh points (or mid-points). As such the applicable accurate methods are somewhat limited. In our situation we chose a third order Simpson method (resulting in a global error of order 4) and it writes as follows

$$\int_{j\Delta x}^{k\Delta x} \zeta(x) dx \approx \Delta x \frac{1}{6} \left(\zeta_j + \zeta_k + 2 \sum_{l=j+1}^{k-1} \zeta_l + 4 \sum_{l=j}^{k-1} \zeta_{l+1/2} \right). \quad (2.14)$$

3 Numerical results

In this part we present a multitude of numerical experiments and simulation results for different one dimensional wave propagation and transformation scenarios. Effects of a solid allowed to move will be compared to a fixed solid case to highlight the main features of this new approach.

As explained in Remark 1.2, the appropriate base water depth for our case is (at least) 10 meters (due to the difference in the order of magnitude of the coefficients). As such, comparable physical experiments are not exactly available.



(a) $\mu = \varepsilon = 0.1$ solitary wave evolution, spatial error (b) $\mu = \varepsilon = 0.1$ solitary wave evolution, temporal error

Figure 3: Discretization error for solitary wave evolution over flat bottom

For our study in general, the wave tank is taken with the following physical parameters: its width is exactly 1000 (meters), its height is $H_0 = 20$. The attributed shallowness parameter is then determined by the choice of the wavelength L , with the two main cases being $L = 40$ for $\mu = 0.25$, and $L = 20\sqrt{10}$ for $\mu = 0.1$. This implies that the wave-tank is 25 wavelengths long in the former case and approximately 16 wavelengths long in the latter case. The principal observational area is in the vertical section $[400, 600]$ of the wave tank.

The solid will be considered to be given by a truncated Gaussian function, the discrete truncation determined by an error term $\epsilon = 10^{-4}$, that is

$$\mathbf{b}(x) = b_0(x)\mathbf{1}(b_0 > \epsilon), \quad \text{where } b_0(x) = a_{bott} \exp\left(-10\left(\frac{x}{L}\right)^2\right).$$

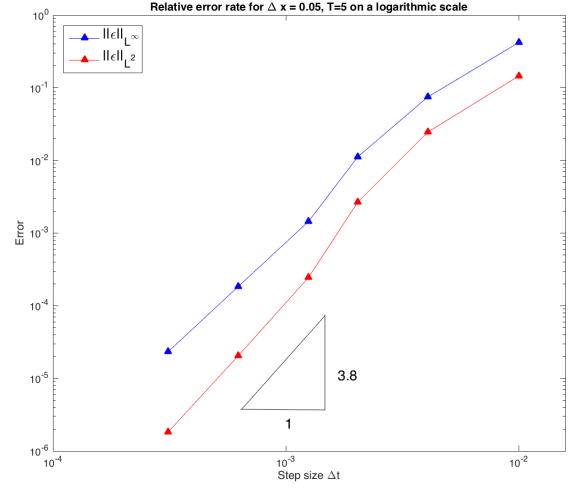
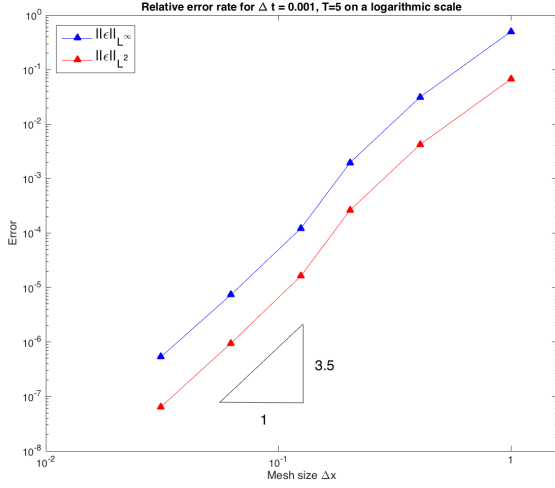
As for its physical parameters, the default choice for the mass parameter is chosen to be $\tilde{M} = \frac{2}{3}$, corresponding to an approximate solid density of $\varrho_S = 2\frac{g}{cm^3}$. The vertical size as well as the coefficient of the friction will be varied during most of the simulations.

3.1 Order of the numerical scheme

The first set of tests concerns the verification of the convergence of the scheme. In [LM07] the overall algorithm for the fluid equations was second order accurate both in time and in space. Since we made some adaptations on the original scheme, it is reasonable to verify how this has affected the order of the convergence. It turns out that considering all situations and parameter regimes relevant to the model we always have a convergence of order at least $\mathcal{O}((\Delta x)^3 + (\Delta t)^2)$.

3.1.1 Convergence of the scheme over a flat bottom topography

First of all, we consider the wave tank without the presence of the solid and its effects. This means that we are considering the simplified algorithm for a flat bottom case. The convergence is then checked numerically by the exact traveling wave solution for (1.2) with $b \equiv 0$. The existence of a solitary wave solution is a well known fact, for explicit computations, please refer to [Che98], for a more general approach, one may see [BC16] for example. By searching the solution for (1.2) as a solitary traveling wave with constant speed $c > 1$ ($\zeta = \zeta_c = \zeta_c(x - ct)$, $\bar{V} = \bar{V}_c = \bar{V}_c(x - ct)$) it is easy to check that the



(a) $\mu = \varepsilon = 0.1$ solitary wave evolution, spatial error (b) $\mu = \varepsilon = 0.1$ solitary wave evolution, temporal error

Figure 4: Discretization error for solitary wave evolution over non-flat bottom ($\beta = 0.3$, $c_{fric} = 0.01$)

velocity profile has to satisfy

$$-(\bar{V}_c)'' = -\frac{3}{\mu c} \bar{V}_c \left(c - \frac{1}{c - \varepsilon \bar{V}_c} - \frac{\varepsilon}{2} \bar{V}_c \right), \quad (3.1)$$

with $\bar{V}_c < c/\varepsilon$. From the velocity profile, the surface elevation then can be recovered simply by

$$\zeta_c = \frac{\bar{V}_c}{c - \varepsilon \bar{V}_c}. \quad (3.2)$$

With this at our disposal, the solitary wave solution serving as a reference can be reconstructed by a fourth order Runge-Kutta method (in order to avoid any influence on the accuracy of the overall scheme).

Two basic verification tests have been designed, each one testing for the wave-tank and wave parameters $\mu = \varepsilon = 0.1$. The simulation is run for a time $T = 1$.

The first test measures the error of the spatial discretization, compared to the solitary wave solution, by fixing the time step Δt sufficiently small ($\Delta t = 0.001$) and varying the spatial discretization's step size, giving us $\Delta x = 2^{-k}$ for $k \in \{0, 1, 2, 3, 4, 5\}$. We measure the L^2 and L^∞ norms of the error for the surface elevation ζ . Figure 3a shows the results, on a logarithmic scale. The scheme is behaving as an algorithm of order 3.5 in the spatial discretization.

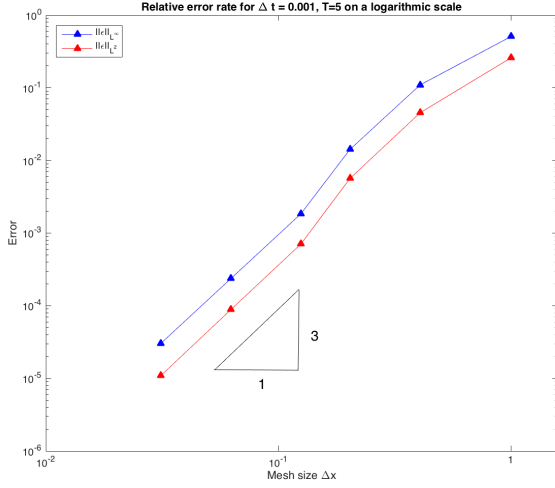
The second test measures the error of the time discretization, compared to the solitary wave solution, by fixing the grid size Δx sufficiently small ($\Delta x = 0.05$) and varying the time discretization's step size, giving us $\Delta t = 0.01 \cdot 2^{-k}$ for $k \in \{0, 1, 2, 3, 4, 5\}$. Once again we measure the L^2 and L^∞ norms of the error for the surface elevation ζ . Figure 3b shows the results, on a logarithmic scale. The scheme is behaving as an algorithm of order 3.8 for the time discretization, an almost order 4 convergence which would be the ideal scenario for the applied Adams predictor-corrector method.

Therefore we have established a major improvement over [LM07], by an accurate interpolation, and more coherent accuracy in the finite difference schemes, one can indeed obtain an almost fourth order convergence.

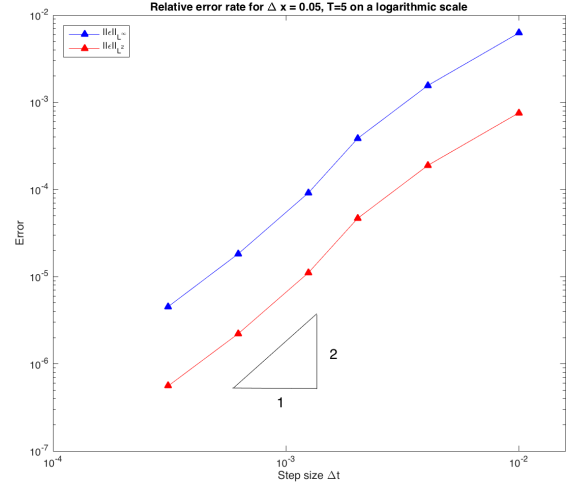
As elaborated in Section 3.4 of [LM07], a von Neumann stability analysis can be carried out for the linearized system. Since no changes have been made in the time discretization of the fluid equations (system (1.2)), their analysis can be adapted in a straightforward way to our case too, leading to a CFL condition of the form:

$$\sqrt{gH_0} \frac{\Delta t}{\Delta x} \leq 0.5. \quad (3.3)$$

In order to respect this stability condition, in what follows we set $\Delta x = 0.05$ and $\Delta t = 0.001$.



(a) Relative spatial error for $\Delta t = 0.001$



(b) Relative temporal error for $\Delta x = 0.05$

Figure 5: L^2 and L^∞ error for a wave evolution over time $T = 5$ ($\mu = \varepsilon = 0.2$, $\beta = 0.4$, $c_{fric} = 0.001$)

3.1.2 Convergence of the scheme for a non-flat bottom topography

Lacking an explicit solution for the non-flat bottom case, we performed a relative error analysis to test the global convergence of the full coupled system as well, meaning that as a reference solution we calculated the surface elevation for $\Delta x = 0.01$, $\Delta t = 10^{-4}$ and we compared it to the calculated surface elevations for less refined mesh sizes and time steps. Two physically different testing parameters were chosen, the first one corresponding to an immobile solid at the bottom, the second one representing the case of the fully coupled problem where solid movement is observed. For the first case, the physical parameters of the system were chosen to be $\mu = \varepsilon = 0.1$, $\beta = 0.3$, with a frictional coefficient of $c_{fric} = 0.01$. The simulation is run for a time $T = 5$.

Figure 4 shows the relative error of the surface elevation compared to our choice of reference solution (in L^2 and L^∞ norms), carried out for either a fixed grid size ($\Delta x = 0.05$) or for a fixed time step ($\Delta t = 0.001$), dividing by 2 the other step parameter for each consecutive measurement, just as before. One can observe that the overall spatial discretization stays of order 3.5, and the temporal error stays in the previously observed order of 3.8 too.

For the second case, the physical parameters of the system were chosen to be $\mu = \varepsilon = 0.2$, $\beta = 0.4$, with a frictional coefficient of $c_{fric} = 0.001$. The simulation is run until a time $T = 5$ allowing for sufficiently long interaction between the solid and the incoming wave.

Figure 5 shows the relative errors (in L^2 and L^∞ norms) for the surface elevation, carried out once again for either a fixed grid size ($\Delta x = 0.05$) or for a fixed time step ($\Delta t = 0.001$). One can observe that the overall spatial discretization has decreased to an order 3, attributed to the loss in accuracy represented by the observable solid motion. Notice also that we have a temporal convergence rate of 2, attributed to the fact that the time discretization scheme for the solid was chosen to be only of order 2.

3.2 Evolution of the surface of a single passing wave

In this part we present the two main characteristic situations that have been observed during the ensemble of the simulations, each with a passing wave and a breaking wave case. Two representative examples were chosen, showing step by step the “transformation” of a single passing wave over the solid, first for a highly frictional case, then for the almost perfect sliding case. As initial conditions, the approaching wave is taken to be the solitary wave solution for the flat bottom case.

3.2.1 The regime of a large coefficient of friction

The first example presents what most of the test cases looked like in the numerical experiments to follow; the wave passing over the solid, getting slightly perturbed by the bottom topography irregularity (the presence of the solid) and continuing its trajectory with a modified amplitude and an altered form. With a shallowness parameter of $\mu = 0.1$, the initial wave amplitude is taken as 4 (meaning $\varepsilon = 0.2$). The solid has a maximal vertical size of 6 and is subjected to a frictional sliding on the bottom, with a coefficient of $c_{fric} = 0.5$.

In Figure 6 this passing wave is plotted (red) at different time steps. As a reference, the flat bottom solitary wave is also visualized (green), propagating at a constant speed, and allowing for a better qualitative comparison for the changes the approaching wave undergoes. The solid is centered around the horizontal coordinate $x = 500$ with a numerical support spanning through the interval $[480, 520]$, for a better visibility, it has been omitted from the figure.

In the first figures the wave approaches the solid, and thus wave shoaling is observed (its amplitude increases) until its peak at around time step 4200, after which the wave crest passes over the peak of the solid and drops (step 5400), due to the drop in the bottom topography. After this drop the initial wave, now slightly asymmetric, continues onward, with an amplitude (slightly) less than its initial value.

Moreover the wave became out of phase due to the “bump” in its motion. One can also observe a backwards going small amplitude long wavelength wave created by the drop after passing over the solid (starting from the back trough at around step 6500). It is important to remark that due to the high frictional term, essentially no solid displacement was observed.

The set of images in Figure 7 depict the wave breaking encountered during the simulations for regimes with a large coefficient of friction. In this case a numerical condition was detected in the experiments that signals a possible wave-breaking due to a steepening wave slope (for more details, see Section 3.4).

A plunging (or spilling) type wave-breaking is most commonly indicated by a critical increase in steepness in the middle section of the front wave slope, and was observed for relatively large wave amplitudes with a large object at the bottom. For a representative test case, a wave of wavelength 40 is chosen over a base water depth of 20, with initial amplitude 7. The solid has a maximal height of 10 and is sliding on the bottom with a dynamical friction coefficient of $c_{fric} = 0.5$. As represented in Figure 7, the wave approaching the solid increases in amplitude, just like before, however this increase becomes critical as the wave crest approaches the solid peak. The flat bottom solitary wave is represented only as a reference.

3.2.2 The regime of a small coefficient of friction

As for a second set of examples, we present a characteristic situation in the regime of small coefficient of friction, that is, when solid displacement is observed. This was observed for all examined vertical solid dimensions, appearing to be more pertinent in intermediate to high wave amplitude regimes. As a test case, we chose $c_{fric} = 0.001$ for a solid height of 8. The wave amplitude is chosen to be 4 with a shallowness parameter of the system equaling $\mu = 0.1$.

As it can be seen from Figure 8 the approaching wave gains amplitude as it starts running up on the slope created by the solid object on the bottom. In this physical scenario the friction term characterizing the solid movement becomes less important than the pressure term, resulting in the solid sliding for a long distance based on the pressure generated by the wave. This solid motion results in a perturbation that creates a new wavefront in front of the solid, thus in front of the initial wave (time step 4000), transmitting its energy to the solid and the newly forming wavefront.

In the meantime the solid starts propagating with increased velocity, thus further amplifying its amplitude (time step 5400). When the wave peak finally passes over the top of the solid, it drops due to the downwards slope in the bottom topography (time step 6000, generating secondary waves traveling backwards (time step 6400). Notice that the passing wave has a significant loss in amplitude (almost 10%) and an attenuated shape (time step 9000).

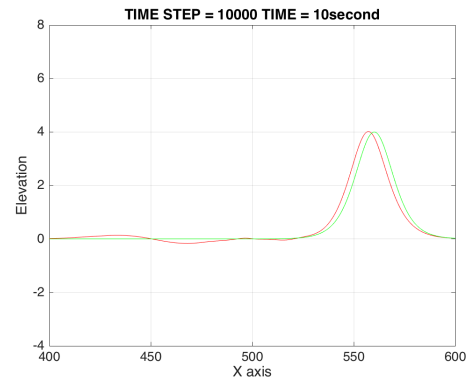
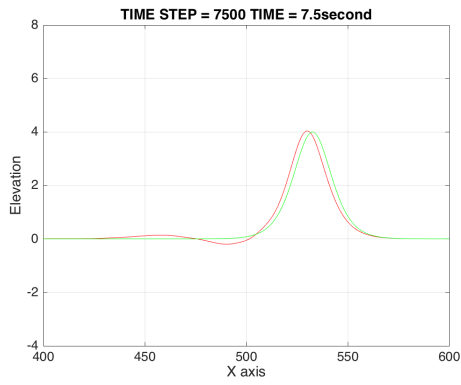
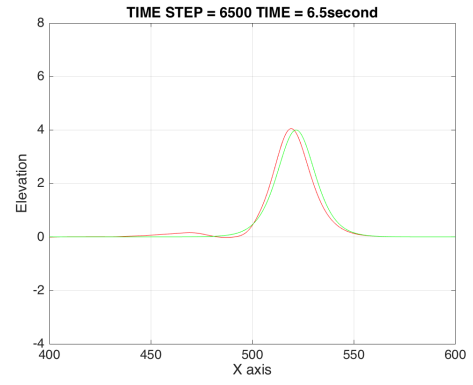
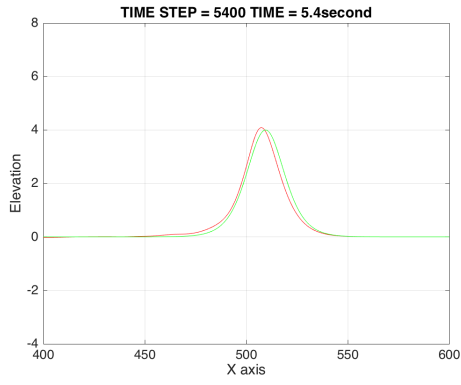
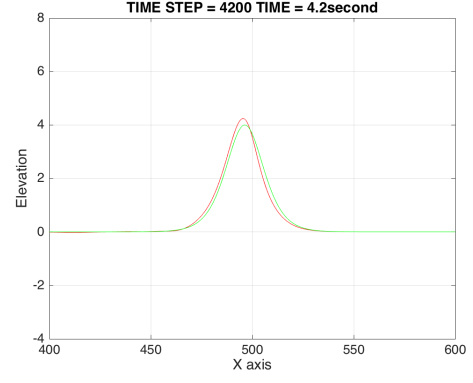
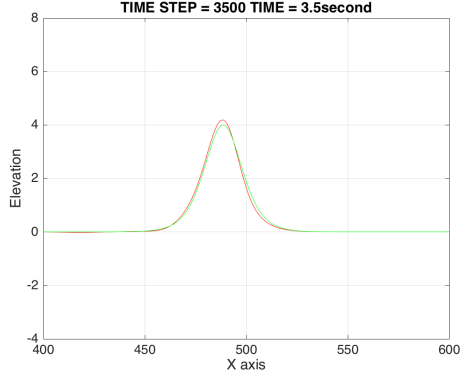


Figure 6: Evolution of a passing wave ($\mu = 0.1$, $\varepsilon = 0.2$) over a small obstacle ($\beta = 0.3$, $c_{fric} = 0.5$); **red** curve is the passing wave, **green** curve is the reference soliton for flat bottom

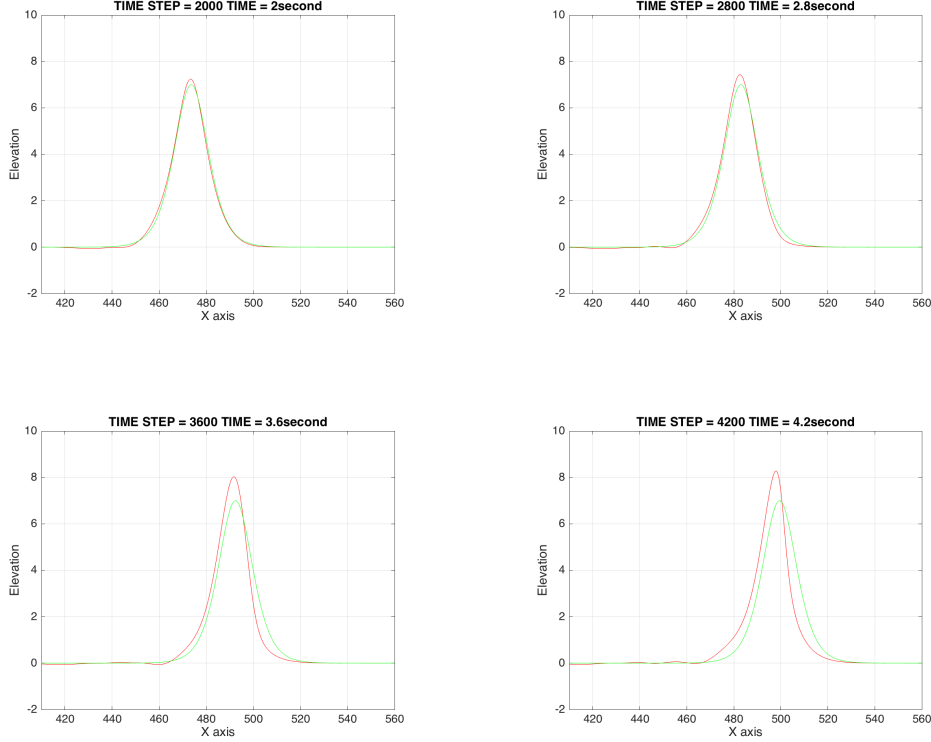


Figure 7: Evolution of an approaching large wave ($\mu = 0.25$, $\varepsilon = 0.35$ and breaking when reaching the obstacle ($\beta = 0.5$, $c_{fric} = 0.5$); red curve is the approaching wave, green curve is the reference soliton for flat bottom

Another type of wave breaking was observed in the nearly perfect, almost frictionless ($c_{fric} \ll 0.01$) sliding cases for large solid objects and intermediate to large wave amplitudes (see Figure 9). The approaching wave gains in amplitude due to the slope presented by the object, further amplified by the fact that the solid starts propagating as well. In these critical cases however, the solid velocity becomes comparable to the passing wave's, thus maintaining the critical position of the wave (time step 4000 – 4500, the wave peak propagates with the solid peak). A solid displacement of 5 to 20 meters can be detected. The critical increase in steepness is detected closer to the front trough, implying a characteristically different wave breaking (surging waves).

3.3 Amplitude variation for a passing wave

The following simulations measure the effect of a bottom topography deformation (a solid object) on a single passing wave, most notably the variation of the amplitude. We will compare the amplitude of a single wave approaching the solid with the amplitude of the same wave after having traversed the interaction zone (that is the section of the water above the object). The main interest is to observe the difference between the cases when the solid is allowed to move and the case where the solid is fixed to the bottom.

A solitary wave for the flat bottom case will be taken as an initial condition, situated two wavelengths from the solid object, traveling towards it. Throughout the simulations a characteristic base wavelength of $L = 40$ is taken for a uniform shallowness parameter of $\mu = 0.25$.

We will consider 3 different (vertical) sizes for the solid, a small object corresponding to $\beta = 0.1$, a medium sized object with $\beta = 0.3$ and a relatively large object for $\beta = 0.5$. For each of these three cases we examine the qualitative effects of the solid. We are testing three different frictional domains as well, an almost frictionless, perfect sliding, with $c_{fric} = 0.001$, a relatively smooth sliding for $c_{fric} = 0.01$, and a hard frictional sliding for $c_{fric} = 0.5$. The results will be compared to the two reference cases: one being

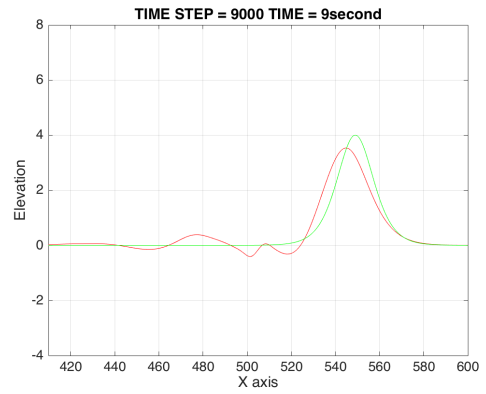
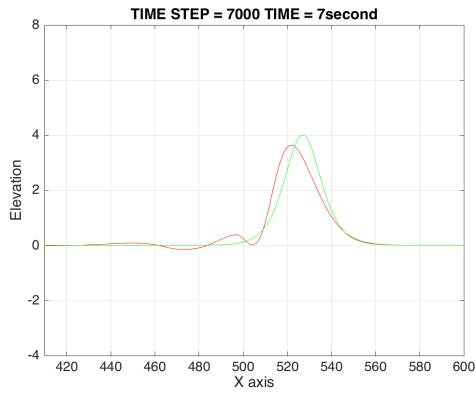
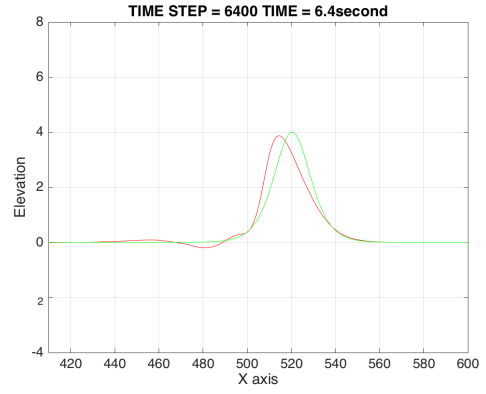
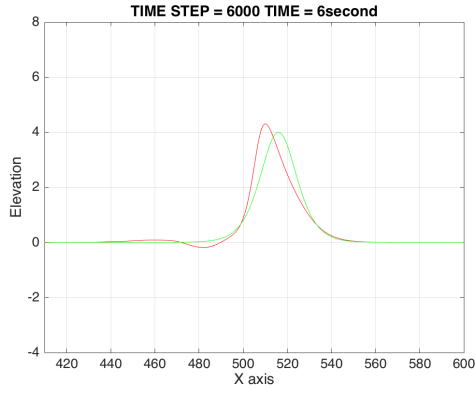
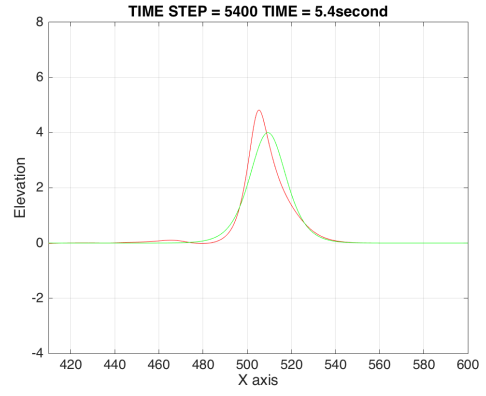
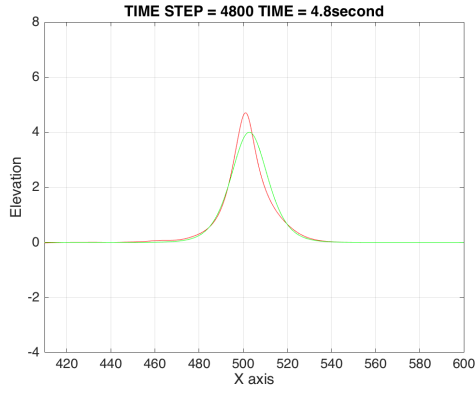
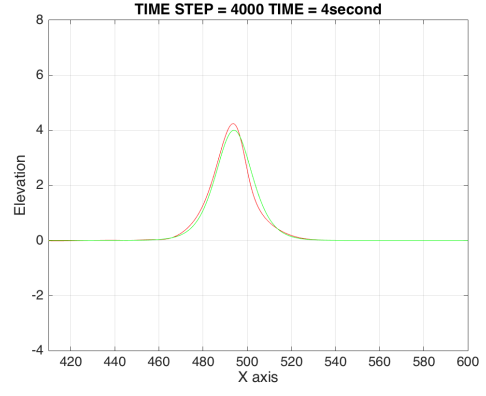
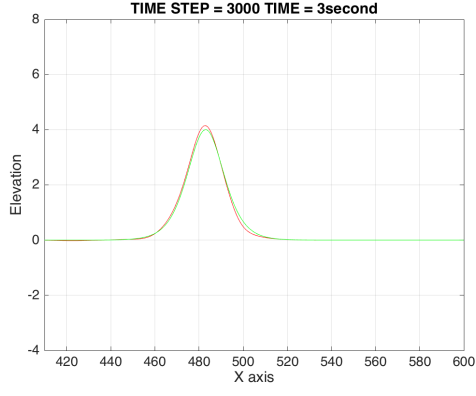


Figure 8: Evolution of a passing wave ($\mu = 0.1$, $\varepsilon = 0.2$) over a larger sliding obstacle ($\beta = 0.4$, $c_{fric} = 0.001$); red curve is the passing wave, green curve is the reference soliton for flat bottom

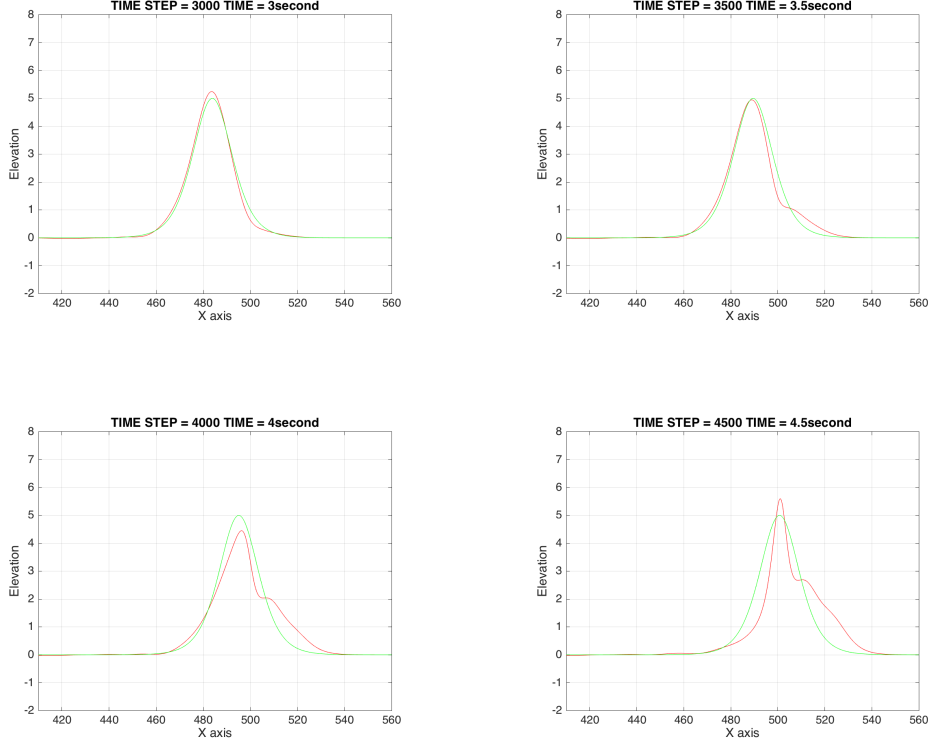


Figure 9: Evolution of an approaching wave ($\mu = 0.25$, $\varepsilon = 0.25$) over an almost perfectly sliding large solid ($\beta = 0.5$, $c_{fric} = 0.001$); red curve is the approaching wave, green curve is the reference soliton for flat bottom

the simulation running for the same time for a flat bottom, giving a 1 to 1 ratio between the entering and the leaving wave amplitude, the other one being the case when the same initial object is fixed to the ground, not being allowed to move throughout the simulation, meaning that $b(t, x) = \mathbf{b}(x)$ independent of the time.

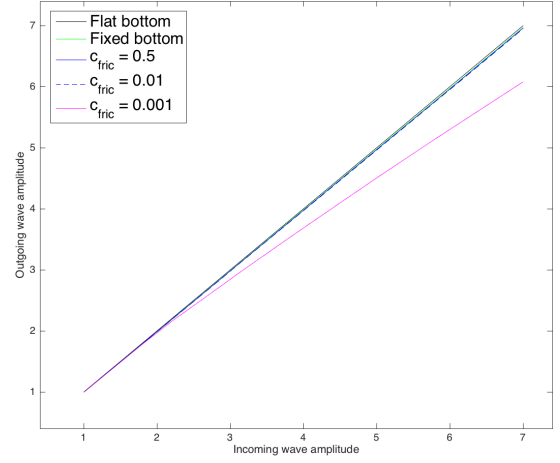
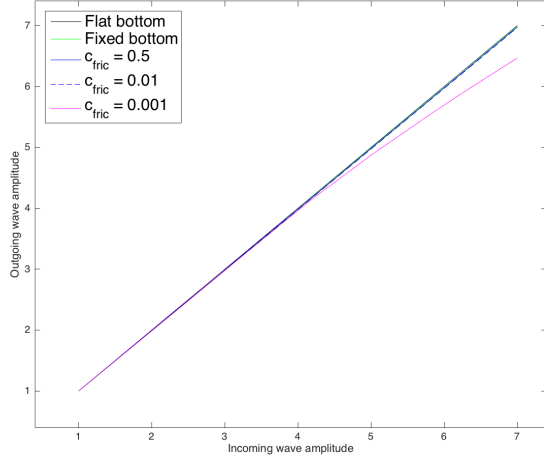
For a small object ($\beta = 0.1$, see Figure 10a) we observe that the 1 to 1 ratio for amplitude variation for a flat bottom is essentially preserved for both the fixed bottom and the cases of a solid with frictional movement with relatively large frictional coefficient. Only an almost negligible (10^{-3}) drop in amplitude is detected in all these situations.

The decrease in amplitude is measurable however in the $c_{fric} = 0.001$ regime for wave amplitudes above 4. This relative drop in amplitude is increased with the increase of the incoming wave height.

For the $\beta = 0.3$ intermediate vertical solid scale, the simulation results are summarized in Figure 10b. One can notice similar effects as the ones concluded in the previous case for a small sized solid. Except for the almost perfect sliding, the other cases respect the 1 : 1 ratio of wave amplitudes.

The impact of the solid is more visible in the almost perfect sliding case, since the considerable drop in amplitude is observed for smaller waves as well. The drop in amplitude amounts for up to 12% amplitude loss for the higher waves. Here we note that for intermediate sized waves, the initial wave is completely absorbed by the new wave produced by the solid motion, which is a longer and much flatter wave (thus the remarkable drop in amplitude). For small wave amplitudes, this is not observed, since the generated pressure force on the bottom is not large enough to create significant solid motion.

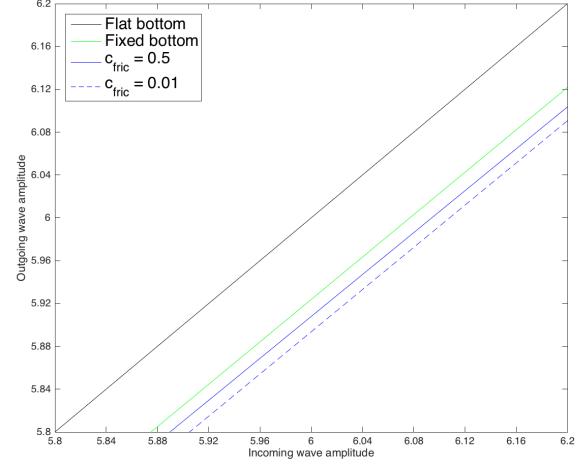
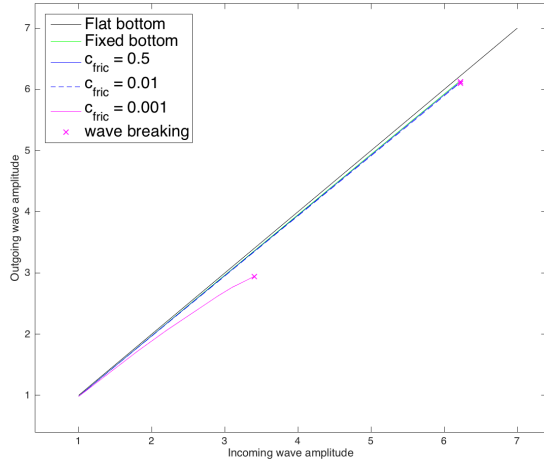
Finally, the results for the $\beta = 0.5$ case (Figure 11) indicate an even more complicated behavior. Amplitude decrease is observed for all the non flat bottom cases, with the drop of the amplitude being more and more important the freelier the object can move (the less friction is imposed). The heavily frictional case ($c_{fric} = 0.5$) still matches quite well the fixed bottom scenario but the other two test cases show a more important decrease in wave amplitude.



(a) Change in wave amplitude over a small solid

(b) Change in wave amplitude over a medium sized solid

Figure 10: Wave amplitude variation for small ($\beta = 0.1$) to medium ($\beta = 0.3$) sized solid ($\mu = 0.25$)



(a) Change in wave amplitude for a passing solitary wave

(b) Zoom to the subcritical section of the amplitudes

Figure 11: Wave amplitude variation for a large ($\beta = 0.5$) solid ($\mu = 0.25$)

Another feature, made clearer in the zoomed image (Figure 11b) is a slight layering between the cases in the presence of a solid, with the fixed bottom case being the closest to preserving the amplitude, closely followed by the hard frictional case, signifying that these two regimes are physically close to each other. Notice that the less important the friction is in the system, the more the amplitude is dropping, especially for middle to high wave amplitudes.

The main difference however is the newfound presence of wave breaking, meaning the simulation was stopped because the numerical condition for the initial wave breaking phase was observed (for more details, please refer to the next section). Not only can we observe wave breaking for all non flat bottom cases, but also there is a slight difference between the fixed and the moving bottom cases too (further examined in the next section).

For the nearly negligible friction ($c_{fric} = 0.001$) surging waves are observed, highlighting the fact that for a larger solid in almost perfect sliding, solid motion can also lead to critical wave transformation. The phenomenon was already described in the last part of the previous section.

To sum it up, we observed that allowing bottom movements, especially for an almost frictionless sliding, accounts for a measurable decrease in wave amplitude. This is due to the fact that part of the energy of the wave is transferred to the solid as a kinetic energy, propelling its motion on the bottom.

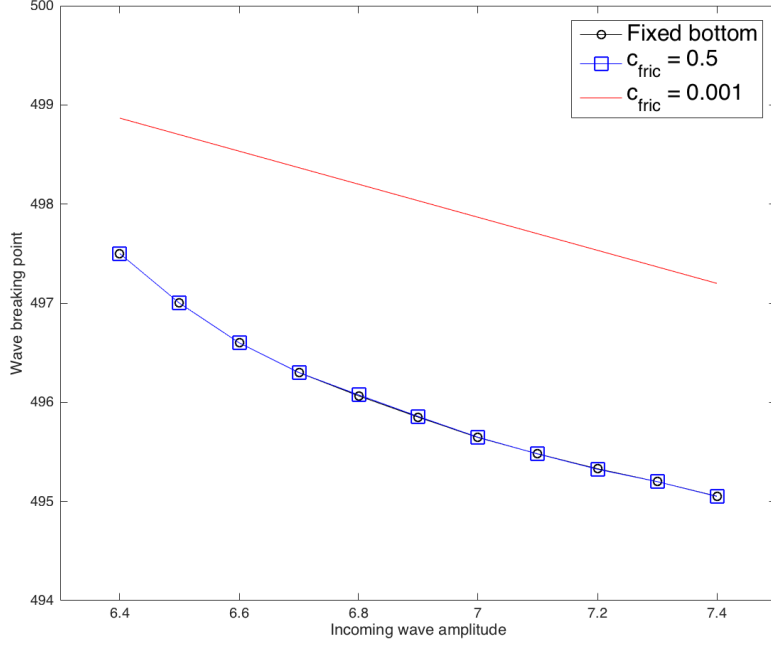


Figure 12: Wave breaking point for large amplitude incoming waves ($\mu = 0.25$, $\beta = 0.5$)

However, in actuality the situation is more complicated, we will address it in Section 3.6. As for the plunging type wave breaking and its correlation with the solid movement, we will address it in what follows.

3.4 An effect on the wave breaking

In this section we summarize the numerical test cases related to the last part of the previous section dealing with the amplitude variation for large solid objects where we observed (plunging type) wave breaking for larger wave amplitudes. It manifested in the fact that the wave became too steep, indicating that physically the wave entered in a wave surging phase, closely followed by the breaking or plunging of the wave. As such the simulation was stopped, even before the wave could pass over the solid.

A sufficient, but rather lenient numerical condition for wave breaking in our case (based on [Sou88]) is the following

$$\max_i \frac{\zeta_{i+1} - \zeta_i}{\Delta x} > 1. \quad (3.4)$$

For a more detailed analysis on wave breaking conditions for Boussinesq type models, we refer to [BCL⁺12] and [KR17].

With a series of experiments we now examine the position of the wave breaking point according to this criteria for different parameter choices. We chose a maximal solid height of $H_0/2$ giving us a topography parameter of $\beta = 0.5$. For this case wave breaking could be observed for large wave amplitudes. We implement two different frictional situations ($c_{fric} = 0.001$, and $c_{fric} = 0.5$), as well as the reference case for a fixed bottom.

A single traveling wave of wavelength $L = 40$ is sent $2L$ distance away from the solid and with a wave amplitude as the principal parameter for the simulations. As a reference, the position of the wave at the moment of the numerical wave breaking point is given by the position of the wave crest. The simulations have also been carried out for the case of a fixed bottom, having the topography of the initial solid state.

The main interest of this numerical experiment was to see the effect of a solid that is allowed to move on the wave breaking point. As it can be seen from the results (Figure 12) the $c_{fric} = 0.5$ frictional case

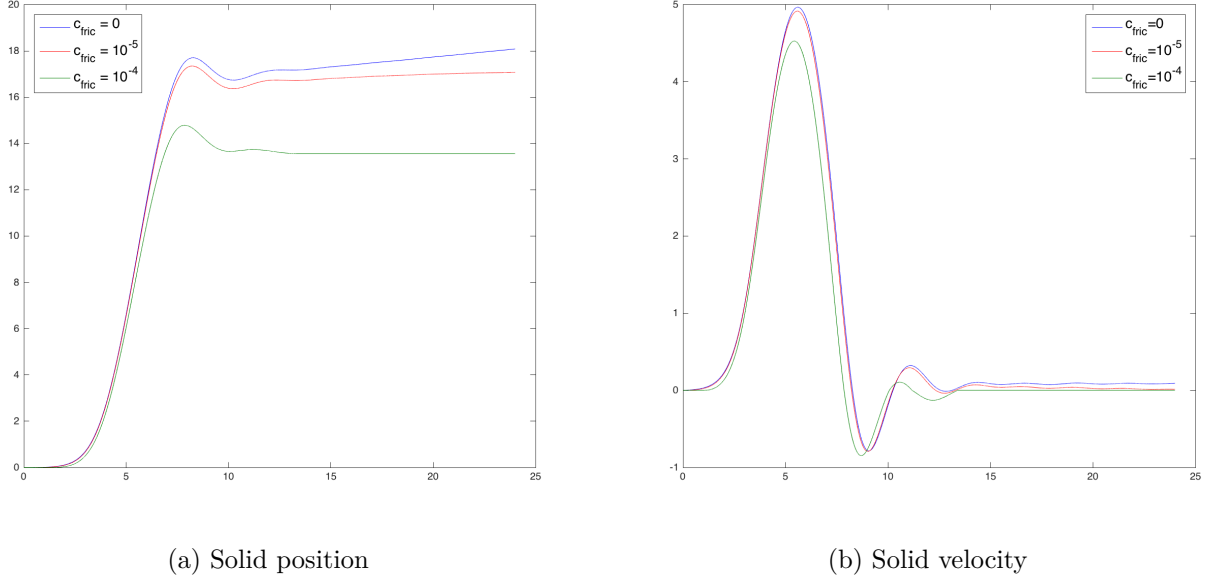


Figure 13: Solid motion for low coefficients of friction ($\mu = \varepsilon = 0.2$, $\beta = 0.4$)

and the fixed bottom barely differ. Actually the same was observed for other c_{fric} values as well (in the range of 0.01 to 1).

In the case when the object is sliding almost frictionlessly ($c_{fric} = 0.001$) however, the position of the wave crest is much further away from the initial position. The qualitative difference is due to the change of the nature of the wave breaking (as it was remarked in Section 3.2). Nevertheless a measurable delay is observed for the wave breaking point, owing to the fact that the initial wave loses some of its energy while the new, frontal wave is created by the solid.

3.5 Observations on the hydrodynamical damping

The previous simulations gave us some insight on the effects of a moving solid on the wave motion. Now we reverse our point of view, so to speak, in order to examine the inverse, that is how the waves affect the solid motion.

Our numerical simulations show that by choosing c_{fric} of order $10^{-4} \sim 10^{-5}$ the solid takes an extended amount of time before finally coming to a halt (Figure 13), creating small amplitude, large wavelength waves in front of and behind it. By creating such waves, its motion is damped by a phenomenon similar to the dead-water phenomenon, described in detail for Boussinesq type models for example in [Duc12].

In the limiting situation of $c_{fric} = 0$ it continues its movement without stopping. Notice the rapidly stabilized oscillatory behaviour in the velocity profile of the solid (Figure 13b), further highlighting the small amplitude wave-generation around the peak of the solid.

The hydrodynamic effects are shown not only by the change in direction for the solid motion as well as the increased changes in velocity. In Figure 14 we compared two situations: as a reference the standard model was left running for the whole time ($T = 24$), for the second simulation the pressure term was removed at the moment when the velocity hit its maximal value, taking into consideration only the frictional damping of the system.

As it can be clearly seen, without the hydrodynamic effects the solid velocity decreases essentially linearly, as it is dictated by the corresponding equation of motion, the solid slowly comes to a halt. The hydrodynamic damping not only increases the deceleration process but it also keeps the solid relatively close to its initial position.

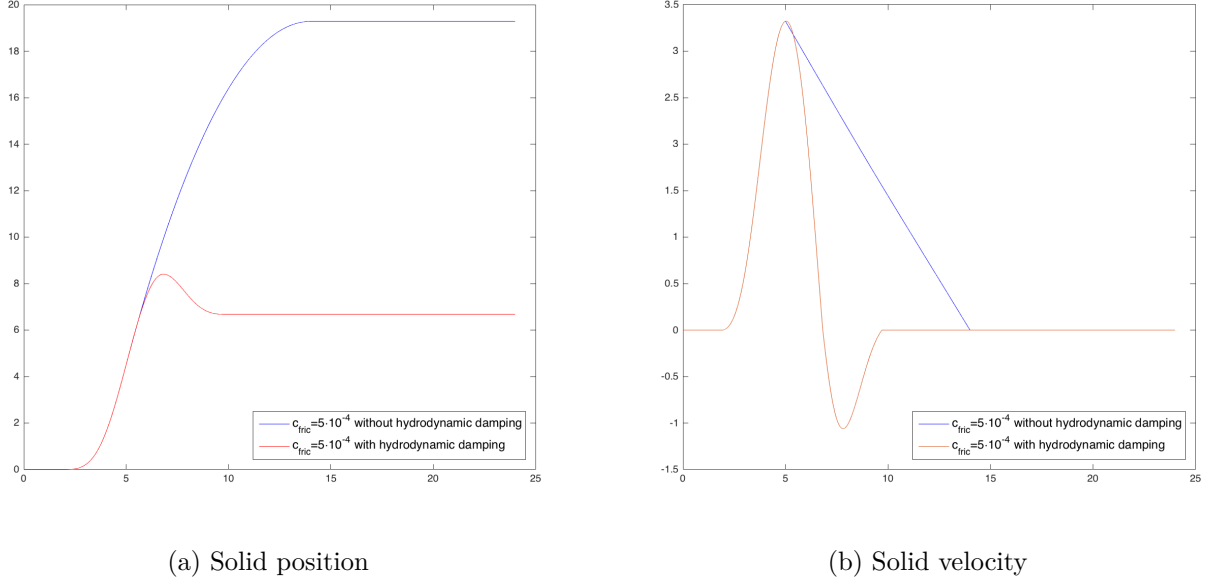


Figure 14: Solid motion with and without hydrodynamic damping ($\mu = \varepsilon = 0.2$, $\beta = 0.4$, $c_{fric} = 0.0005$)

3.6 Measurements of the solid displacement

Three additional sets of simulations were conducted in order to measure the effects of friction on the system, as well as to highlight long term effects by means of simulating an approaching wave train.

3.6.1 Solid displacement for varying coefficients of friction

The first set of tests was conducted in tandem with the observations on the wave surging for almost perfect sliding. For the physical parameters $\beta = 0.3$ and $\varepsilon = 0.25$ the friction coefficient is varied from 0.001 to 0.003. Figure 15 shows the change in the solid motion for this case.

We remark a significant drop in the maximal solid displacement, attributed to the qualitative change of the system from a frictional to a frictionless sliding. The critical values for c_{fric} for this transformation depend on the shape of the object as well as its physical parameters.

Furthermore we remark that the solid does in fact stop in its motion, a property due to not only the damping effect of the frictional forces but to the hydrodynamic damping as well. The latter one is clearly visible by the fact that the solid motion changes direction after the wave peak passes over it and rapidly loses velocity by the time the wave leaves the interaction zone.

3.6.2 Solid displacement for varying wave amplitudes

The second one consists of measuring the effect of a single traveling wave on the solid motion, for a relatively frictionless sliding ($c_{fric} = 0.001$). The maximal vertical size of the solid is 6, with waves having an amplitude in the range $[3, 5]$. It also serves as a reference case for the wave train simulations presented later on.

On Figure 16 we can see the almost perfect “oscillation circle” for the solid position, meaning that after the approaching wave pushes the solid forward, it passes over the object, and then it pushes the solid backwards, making it return nearly to its initial state. Notice the slight asymmetry of the curves as well as the rather extended calming phase, attributed mainly to the slowing effects of frictional forces.

The final set of numerical experiments concerns the long term effects of wave motion on a solid that is allowed to move freely, subjected to a frictional sliding on the bottom of the wave tank. This was carried out by simulations on a long time scale, it involves sending a wave train consisting of 10 consecutive solitary waves in the direction of the solid and measuring the evolution of the solid displacement.

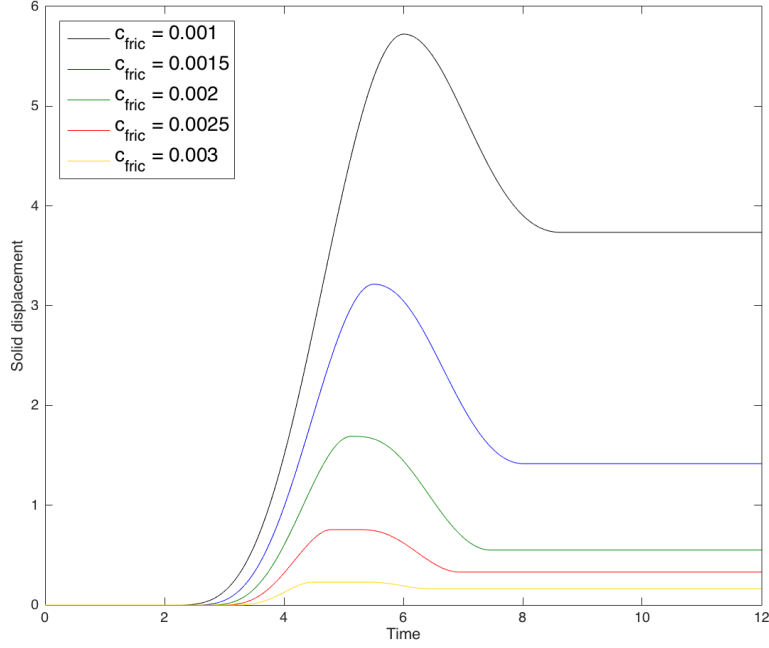


Figure 15: Solid displacement for a varying coefficients of friction ($\mu = \varepsilon = 0.25$, $\beta = 0.3$)

The wave tank is now taken to be twice as large as before, with a length of 2000 to properly accommodate the wave train. A medium sized solid is chosen ($\beta = 0.3$) for intermediate wave amplitudes (ε ranging from 0.15 to 0.25) with a wavelength of $L = 40$. The simulation is run for a time of $T = 54$, allowing for 7 waves to pass over the solid.

The evolution of the position of the center of the mass is plotted in Figure 17, corresponding to an almost perfect sliding ($c_{fric} = 0.001$). We observe solid displacement of order 1 for each passing wave, as well as some qualitative differences in the wave cycles.

There is a positive net solid displacement per incoming wave, resulting in the solid getting further and further away from the initial position after each passing wave in the train. We remark that the displacement per passing wave is not constant, attributing to an overall nonlinear increase in distance. This is due to the fact that a passing wave is perturbed by the solid, resulting in backwards traveling small amplitude long waves (as pointed out in Section 3.2), meaning that later members of the wave train get perturbed even before reaching the interaction zone. This results in a non-constant incoming wave amplitude even though initially it was constant.

Also, comparing the effects of a single wave (Figure 16) with a wave train (Figure 17), we can notice that, even though the elements of the wave train were launched sufficiently apart to avoid undesired interactions with each other, due to the extended period of time it takes for the frictional and hydrostatic damping to slow down the solid motion, nonlinear effects are observable in the solid displacement.

4 Conclusion

In the present paper, we complemented the author's previous, mostly theoretical work ([Ben17]) by a numerical analysis of relevant shallow water situations. A staggered grid based finite difference method incorporating an Adams predictor-corrector algorithm ([LM07]) was adapted to the coupled Boussinesq equations. A numerical verification indicates a convergence of order three in space and an order two in time variable. We not only showed that the motion of the solid reduces the wave amplitude in general, but also that it affects the wave breaking. We observed the presence of surging type wave breaking for low friction regimes as well as nonlinear interactions between the wave propagation and the solid displacement.

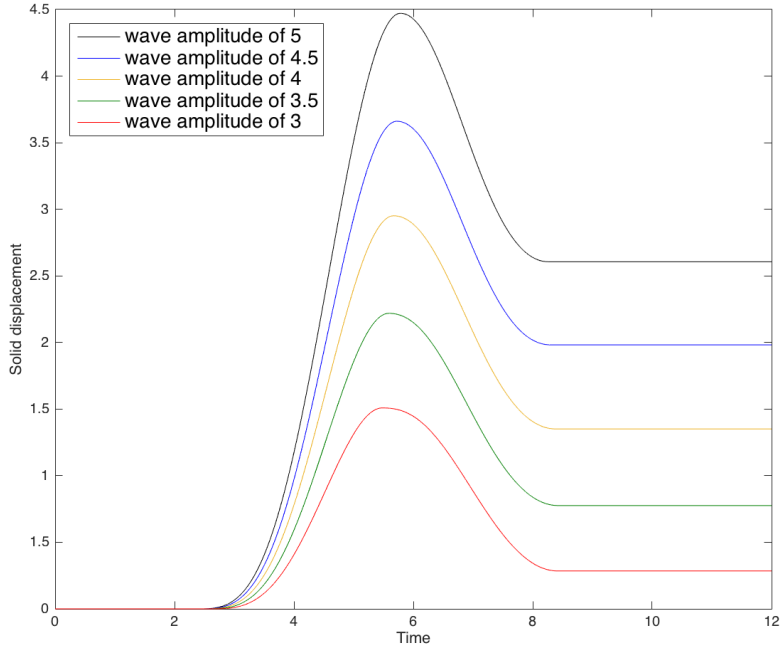


Figure 16: Evolution of the solid position due to a single solitary wave, with frictional sliding ($\mu = 0.25$, $\beta = 0.3$, $c_{fric} = 0.001$)

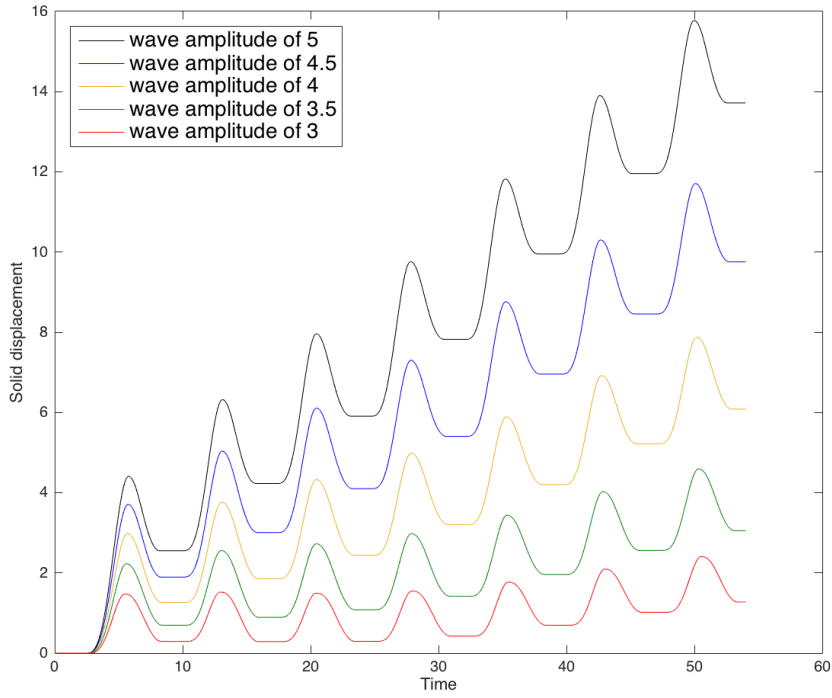


Figure 17: Evolution of the solid position due to a wave train, with almost perfect sliding ($\mu = 0.25$, $\beta = 0.3$, $c_{fric} = 0.001$)

References

- [ACDn17] Stéphane Abadie, Marcela Cruchaga, Benoit Ducassou, and Jonathan Nuñez. A fictitious domain approach based on a viscosity penalty method to simulate wave/structure interaction. *Journal of Hydraulic Research*, pages 1–16, 2017.
- [AELS14] Reza Alam, Ryan Elandt, Marcus Lehmann, and Mostafa Shakeri. The Wave Carpet: Development of a Submerged Pressure Differential Wave Energy Converter, 2014. 30th Symposium on Naval Hydrodynamics, Hobart, Australia.
- [AMMM15] Stéphane Abadie, Manuel Martin Medina, Cyril Mokrani, and Denis Morichon. Déplacement d’une structure soumise à l’impact d’un front d’onde, 2015. Rencontres Universitaires de Génie Civil.
- [BC16] Stevan Bellec and Mathieu Colin. On the existence of solitary waves for Boussinesq type equations and a new conservative model. *Advances in Differential Equations*, 21:945–976, 2016.
- [BCL⁺12] Philippe Bonneton, Florent Chazel, David Lannes, Fabien Marche, and Marion Tissier. A new approach to handle wave breaking in fully non-linear Boussinesq models. *Coastal Engineering*, 67:54–67, 2012.
- [BCS02] Jerry Lloyd Bona, Min Chen, and Jean-Claud Saut. Boussinesq equations and other systems for small-amplitude long waves in nonlinear dispersive media. i: Derivation and linear theory. *Journal of Nonlinear Science*, 12:283–318, 2002.
- [Ben17] Krisztián Benyó. Wave-structure interaction for long wave models with a moving bottom, 2017. preprint.
- [Boc18] Edoardo Bocchi. Floating structures in shallow waters: local well-posedness in the axisymmetric case, 2018. preprint; hal-01714437.
- [Bou71] Joseph V. Boussinesq. Théorie générale des mouvements qui sont propagés dans un canal rectangulaire horizontal. *Comptes Rendus des Séances de l’Académie des Sciences, Paris*, 73:256–260, 1871.
- [Che98] Min Chen. Exact traveling-wave solutions to bidirectional wave equations. *International Journal of Theoretical Physics*, 37(5):1547–1567, 1998.
- [Che03] Min Chen. Equations for bi-directional waves over an uneven bottom. *Mathematics and Computers in Simulation*, 62:3–9, 2003.
- [CM06] Georges-Henri Cottet and Emmanuel Maitre. A level set method for fluid-structure interactions with immersed surfaces. *Mathematical Models and Methods in Applied Sciences*, 16:415–438, 2006.
- [CMM08] Georges-Henri Cottet, Emmanuel Maitre, and Thomas Milcent. Eulerian formulation and level set models for incompressible fluid-structure interaction. *ESAIM: Mathematical Modelling and Numerical Analysis*, 42(3):471–492, 2008.
- [DK13] Denis Dutykh and Henrik Kalisch. Boussinesq modeling of surface waves due to underwater landslides. *Nonlinear Processes in Geophysics*, 20:267–285, 2013.
- [DNZ15] Denys Dutykh, Hayk Nersisyan, and Enrique Zuazua. Generation of two-dimensional water waves by moving bottom disturbances. *IMA Journal of Applied Mathematics*, 80(4):1235–1253, 2015.
- [Duc12] Vincent Duchêne. Boussinesq/Boussinesq systems for internal waves with a free surface, and the KdV approximation. *ESAIM: Mathematical Modelling and Numerical Analysis*, 46(1):145–185, 2012.

- [Ekm04] Vagn Walfrid Ekman. On dead water. *Scientific Results of the Norwegian North Polar Expedition 1893-1896*, 5(15):1–152, 1904.
- [FGG07] Miguel A. Fernández, Jean-Frédéric Gerbeau, and Céline Grandmont. A projection semi-implicit scheme for the coupling of an elastic structure with an incompressible fluid. *International Journal for Numerical Methods in Engineering*, 69:794–821, 2007.
- [GIL⁺14] Mateus das Neves Gomes, Liércio André Isoldi, Max Letzow, Luiz Alberto Oliveira Rocha, Elizaldo Domingues dos Santos, Flávio Medeiros Seibt, and Jeferson Avila Souza. Computational modeling applied to the study of wave energy converters (WEC). *Marine Systems and Ocean Technology*, 9:77–84, 2014.
- [GN07] Philippe Guyenne and David P. Nicholls. A high-order spectral method for nonlinear water waves over moving bottom topography. *SIAM Journal of Scientific Computing*, 30(1):81–101, 2007.
- [HI15] Fujiwara Hiroyasu and Tatsuo Iguchi. A shallow water approximation for water waves over a moving bottom. *Advanced studies in pure mathematics*, 64:77–88, 2015.
- [Igu11] Tatsuo Iguchi. A mathematical analysis of tsunami generation in shallow water due to seabed deformation. *Proceedings of the Royal Society of Edinburgh Section A: Mathematics*, 141:551–608, 2011.
- [KR17] Maria Kazolea and Mario Ricchiuto. On wave breaking for Boussinesq-type models, 2017. Research Report: hal-01581954.
- [Lan13] David Lannes. *The water waves problem: mathematical analysis and asymptotics*, volume 188 of *Mathematical Surveys and Monographs*. American Mathematical Society, 2013.
- [Lan17] David Lannes. On the dynamics of floating structures. *Annals of Partial Differential Equations*, 3(1), 2017.
- [LM07] Pengzhi Lin and Chuanjian Man. A staggered-grid numerical algorithm for the extended boussinesq equations. *Applied Mathematical Modelling*, 31(2):349–368, 2007.
- [Mit09] Dimitrios E. Mitsotakis. Boussinesq systems in two space dimensions over a variable bottom for the generation and propagation of tsunami waves. *Mathematics and Computers in Simulation*, 80(4):860–873, 2009.
- [MVD10] Matthieu Mercier, Romain Vasseur, and Thierry Dauxois. Resurrecting dead-water phenomenon. *Nonlinear Processes in Geophysics*, 18:193–208, 2010.
- [Nwo93] Okey Nwogu. Alternative form of Boussinesq equations for nearshore wave propagation. *ASCE Journal of Waterway, Port, Coastal, and Ocean Engineering*, 119(6):618–638, 1993.
- [Per67] D. Howell Peregrine. Long waves on a beach. *Journal of Fluid Mechanics*, 27(4), 1967.
- [Sou88] Howard Neil Southgate. Wave Breaking - a review of techniques for calculating energy losses in breaking waves, 1988. Technical Report, Hydraulics Research Wallington.
- [TW92] Michelle H. Teng and Theodore Y. Wu. Nonlinear water waves in channels of arbitrary shape. *Journal of Fluid Mechanics*, 242:211–233, 1992.
- [Wu87] Theodore Y. Wu. Generation of upstream advancing solitons by moving disturbances. *Journal of Fluid Mechanics*, 184:75–99, 1987.